Control of a MEMS Fast Steering Mirror for Laser Applications

by

Joseph Kerivan Lane

Submitted to the Department of Electrical Engineering and Computer Science
in Partial Fulfillment of the Requirements for the Degree of

Master of Engineering in Electrical Engineering and Computer Science

at the Massachusetts Institute of Technology

May 2012
[JUNE 2012]

Author .....
Department of Electrical Engineering and Computer Science
May 21, 2012

Certified by .....
Prof. James K. Roberge
Professor of Electrical Engineering
Thesis Supervisor

Certified by ..
Dr. Gary Shaw
Senior Staff, MIT Lincoln Laboratory
Thesis Co-Supervisor

Accepted by ..
Prof. Dennis M. Freeman
Master of Engineering Thesis Committee
Chairman

Control of a MEMS Fast Steering Mirror for Laser Applications

by

Joseph Kerivan Lane

Submitted to the Department of Electrical Engineering and Computer Science

May 21, 2012

In partial fulfillment of the requirements for the degree of
Master of Engineering in Electrical Engineering and Computer Science

Abstract

A control system for a MEMS fast steering mirror is designed and implemented to accurately steer a laser beam. This document contains a characterization of important mirror characteristics and the full analysis of an analog control system designed to maximize the performance of the mirror. A full analysis of the performance of the design, including bandwidth, stability, accuracy, power consumption, and system size and weight, is provided along with optical scan expansion designs. Finally, future possible improvements to the design are discussed.

Thesis Supervisor: Prof. James K. Roberge
Title: Professor of Electrical Engineering

Thesis Co-Supervisor: Dr. Gary Shaw
Title: Senior Staff MIT Lincoln Laboratory

Acknowledgments

First, I would like to thank Professor J. K. Roberge, my supervisor for the project and the source of inspiration for many of the ideas throughout this thesis. Professor Roberge first approached me after my initial presentation on the project to offer his guidance and support. Through his conversations and teachings has come my sincere enjoyment of the topic.

I would also like to thank Dr. Gary Shaw, my advisor at Lincoln Laboratory. Without his hard work and supervision this project would likely not have been a success.

There are many people at Lincoln Laboratory who have helped me along the way. Thank you to all of Group 99 for making my time at Lincoln truly fun and enjoyable. I would like to acknowledge Dr. Andrew Siegel. Andy was always available to discuss analog design and any topic of interest.

To all my friends and family, I sincerely appreciate your support.

Contents

List of Figures

Chapter 1

Introduction

Laser based technology is becoming more important for critical military and civil applications such as imaging, communications, and range estimation [1]. Optical systems offer an inherent advantage over radio frequency (RF) systems due to the relatively high frequency and narrow beam width of optical signals, enabling a higher percentage of the transmit power concentrated on the target receiver. Better transmission efficiency enables any transmission and receiving electronics to be made smaller, lighter, and lower power [2]. Additionally, the use of optical frequency bands is not regulated like RF bands and the small beam width of optical signals minimizes the risk of unwanted detection. By replacing RF systems with optical technology, a mobile system, such as a satellite or robotic platform, can potentially be made smaller, lighter weight, and more power efficient.

Probably the most significant precursor to modern day optical communication systems was invented by Alexander Graham Bell in 1880, a device that Bell called the Photophone. The Photophone worked by utilizing a mechanical transducer to convert acoustic pressure waves into modulations of a reflective mirror. Light reflected off the mirror would then be picked up and translated into an electrical signal by crystalline selenium cells that exhibit a resistance inversely proportional the amount of incident light on their surface [3]. While Bell's Photophone never caught on, the invention of the laser in the 1960's sparked new interest in optical communication and imaging.

Today, there are two popular methods for transmitting and receiving optical signals; through optical fiber and over free space. Fiber optic cables enable efficient and low interference transmission of optical signals and remain the backbone of current Internet, television, and telephone services. Like fiber optic systems, free space optical systems are also very efficient, benefiting from recent advancements in photo-detectors and high capacity coding schemes. For example, research at MIT has lead to the development of high resolution solid-state photon counting detectors, such as Gieger-

mode avalanche and super-conducting photo-detectors. Coupled with advanced "turbo" codes and iterative decoders, transmission rates approaching the fundamental limit proposed by the Shannon-Hartley theorem can be achieved [4, 5].

While advancements in photon detection and channel encoding have enabled ultra-fast links, the fundamental problem of pointing a laser beam with very high accuracy and precision remains a challenge. In the case that the platform is mobile, a beam steering system must be able to function properly in the presence of vibration as well as under translation and rotation of the platform. In 1990, MIT Lincoln Laboratory's Gregory Loney designed a high bandwidth beam steering mirror assembly [6]. Shown in Figure 1.1, Loney's fast steering mirror (FSM) operates using four voice coil actuators acting on a small circular mirror attached through a flexure assembly. Much like how a speaker driver pushes and pulls a speaker cone to generate sound, each voice coil applies complementary torque to the four sides of the mirror to rotate the mirror to a desired position. Two different types of position sensors were incorporated into Loney's design. The first sensor operates by using a small coil to emit a fluctuating magnetic field onto a conductive surface placed on the back of the mirror, generating eddy currents in the surface. The strength of the eddy currents are then used to estimate the angular position of the mirror. The second position sensor is a photo-diode quadrant detector placed external to the mirror. A fraction of the beam is deflected onto the quadrant detector, generating four voltages proportional the area of the beam incident on each quadrant. All together, the FSM is able to achieve a closed-loop bandwidth of 10kHz with a resolution of 0.2μrad over a range of 26mrad. However, due to the mirror's size, the assembly consumes roughly 1W and weighs 0.7kg.

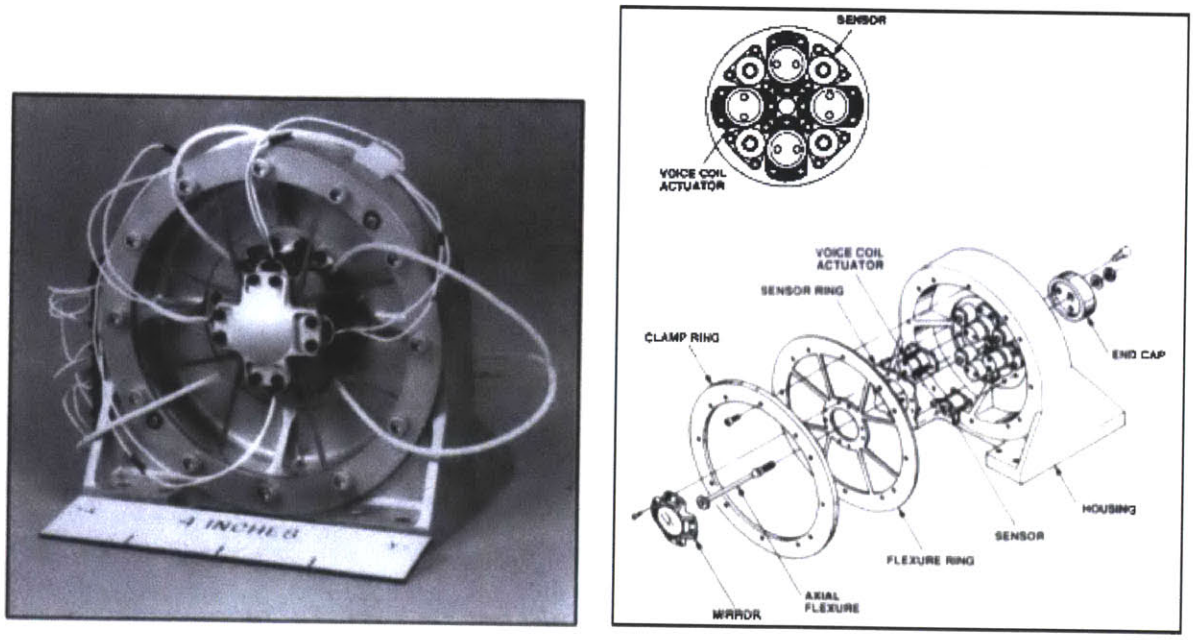

(a) Fully assembled FSM designed by G. Loney at MIT Lincoln Laboratory in 1990 [6]

(b) Exploded view of Loney's FSM [6]

Figure 1.1: Original Lincoln Laboratory fast-steering mirror

Like Loney's original design, many of today's typical beam steering devices include a large mirror assembly or implement a mechanical gimbal design [6, 7, 8]. For example, the most popular fast steering mirrors remain galvanometer systems in which a servomechanism rotates a mirror along one dimension [7]. Thus, in order to steer a beam over two dimensions, two different mirror assemblies are required. The size, weight, and power constraints of today's mobile applications can limit the usefulness of such systems. As a potential solution, fast steering mirrors have recently been designed using techniques in micro-electromechanical system (MEMS) manufacturing [9].

Current micro-fabricated fast steering mirrors can be separated into two categories based on their drive mechanisms: electro-static and magnetic. Electro-static drives implement either a comb drive or parallel plate system whereby torque is applied to the mirror structure via electro-static forces. Two examples of comb drive systems incorporating lateral and vertical comb drives are shown in Figures 1.2(a) and 1.2(b), respectively. The advantages of electro-static MEMS is that they offer small, lightweight, low power, and high bandwidth operation. However, they often lack internal position sensing, potentially suffer from nonlinear drive dynamics, and frequently require high ($>$ 100V) operating voltages. Magnetic drives include essentially a miniaturized inductive coil system similar to the one found in Loney's original design. Pairs of magnetic material and inductive voice coils are constructed to steer the mirror surface [7]. This technique is utilized in the Texas

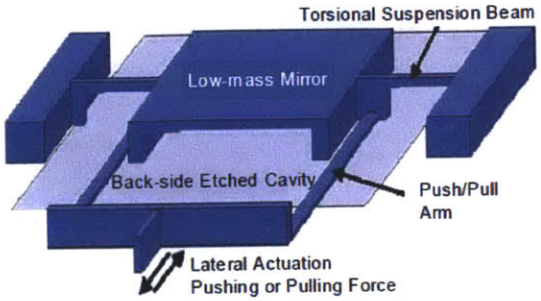

(a) Lateral comb drive model [9]

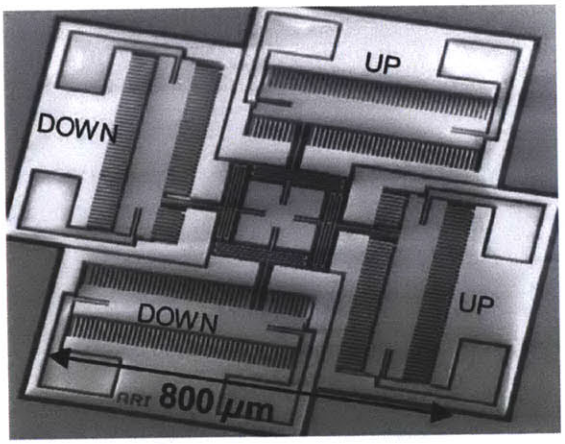

(b) Vertical comb drive model [10]

Figure 1.2: Variants of electro-static MEMS drive systems

Instruments TALP1000b micro-mirror, the system of interest for this project. In contrast to electro-static drive mechanisms, magnetic systems have the advantage of a very linear drive response, can achieve relatively large deflection angles, and have the space necessary to integrate on-board position sensing.

The Texas Instruments TALP1000b micro-mirror was chosen for this project for its large angular deflection range, internal position feedback, and low operating voltages. As will be discussed, the mirror has a sharp resonant peak at roughly 130Hz resulting in a slow and underdamped system. In order to improve input command tracking and high frequency operation, a feedback control system is designed and implemented.

Chapter 2 introduces the operation and dynamic characteristics of the mirror, emphasizing characteristics important to the control design. Chapters 3 gives an overview of the instruments and techniques used to accurately measure the optical and electro-mechanical characteristics that are discussed in Chapter 4. Next, chapter 5 provides the analysis and implementation of an analog controller. Chapter 6 gives an overview of possible beam angle expansion techniques. Finally, Chapter 7 covers potential areas for further improvement and a summary of completed work.

Chapter 2

MEMS Mirror Device

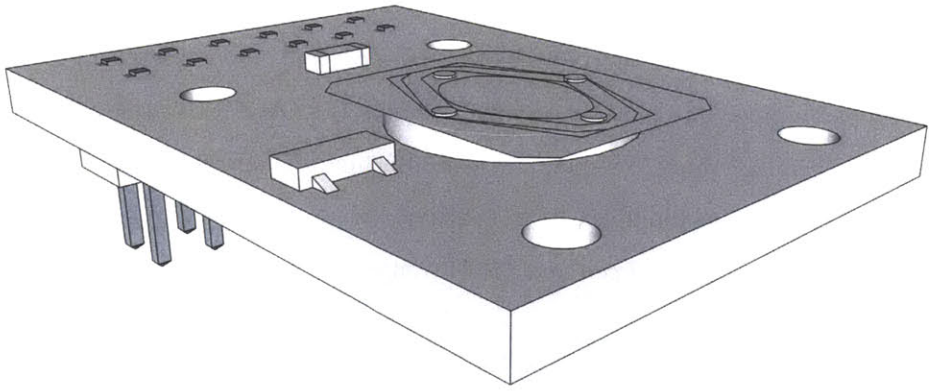

Figure 2.1: TALP1000b 3D Model

The Texas Instruments TALP1000B fast steering micro-mirror is utilized throughout this project. In this chapter, an overview of the functionality of the mirror is given including the hardware necessary to obtain basic steering operation.

2.1 Theory of Operation

The mirror assembly is built on top of a ceramic circuit board measuring 16mm by 23.5mm. Located on the board is a 0.1μF bypass capacitor, a small analog temperature sensor, and finally the mirror and position feedback hardware. The temperature sensor can be used to calibrate the mirror as the impedance of the voice coils and the responsiveness of the position feedback hardware changes under varying temperatures. A 3-D model of the mirror can be seen in Figure 2.1.

The surface of the mirror consists of three different sections. A static outer backplane makes up the first section. The backplane serves primarily to dissipate heat and to shade the quad cell from

any ambient light. Moving toward the center of the assembly is an outer frame that is connected to the backplane through two thin connections at the horizontal corners of the frame. Inside the outer frame is the mirror surface that is attached to the outer frame by two thin connections at the vertical corners of the mirror. A permanent magnet is fixed on the horizontal corners of the center mirror and the vertical corners of the outer frame. Finally, underneath each magnet lies a voice coil that is connected as a complementary pair with the coil on the opposite corner. As current is applied to each complementary pair of coils, a magnetic field is induced that applies a torque on the above magnets. Thus, the horizontal and vertical axes are controlled by varying the amount of current through each pair of voice coils. At $\pm 5°$, the maximum mechanical rotation angle of each axis, each coil pair requires approximately 65mA of drive current. With a resistance of 65Ω at room temperature, each coil pair consumes roughly 275mW at maximum rotation.

There are a number of different methods for obtaining angular measurements of the mirror surface. In Loney's original design, two different types of sensors were used; an on-board eddy current sensor and an off-board photo-diode quad cell. In a similar manner, the TALP1000b assembly accomplishes integrated position feedback through a quad cell placed behind the mirror surface. The quad cell is illuminated by a small LED centered in between each quadrant of the quad cell. Figure 2.2 shows a three dimensional model of the quad cell and LED arrangement.

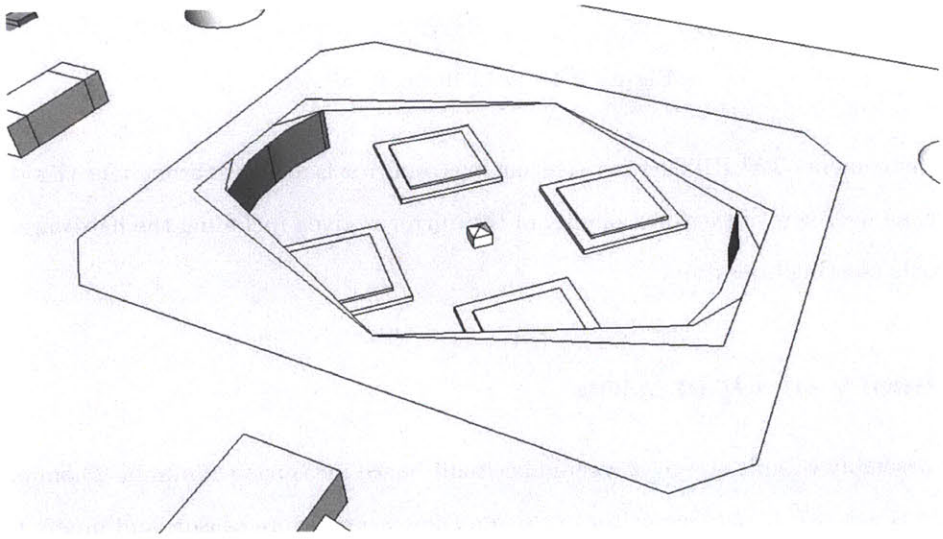

Figure 2.2: Model of the Integrated Position Feedback (IPF) quad cell and LED

Typical quad cell arrangements try and place each quadrant of the quad cell as close together as possible in order to achieve linear tracking of a laser spot over the boundaries of each quadrant. As shown in Figure 2.2, the quadrants have been placed a significant distance apart. To compensate

for this, the LED disperses its light such that when the mirror is centered, each quadrant receives equal excitation. This design suffers from slightly larger nonlinearities compared to standard quad cell arrangements in which the quadrants are nearly adjacent. Additionally, each quadrant is placed in close proximity to the open edges of the backplane resulting in extra sensitivity to ambient light noise. A full electronic schematic of the mirror is shown in Figure 2.3.

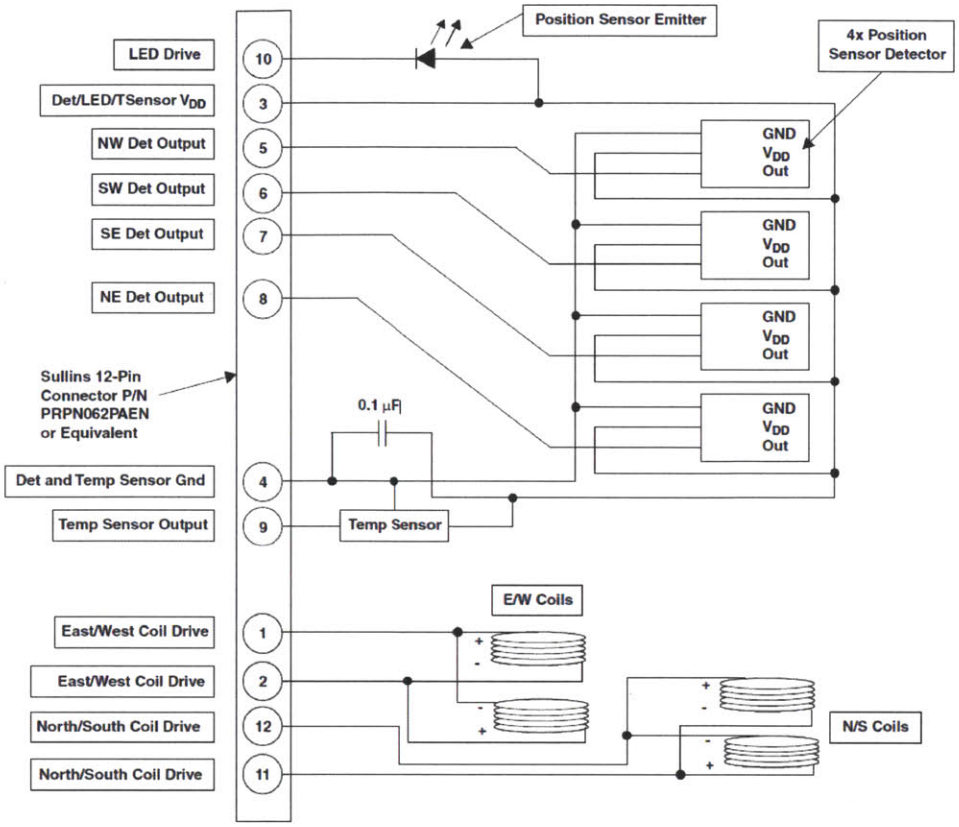

Figure 2.3: Mirror board electronic schematic

A summary of the primary specifications as listed by Texas Instruments is shown in Table 2.1.

Parameter	Min	Typical	Max
Supply Voltage	4.8		5.2V
Mechanical Rotation		±5°	
Mirror Resonant Frequency	112Hz		152Hz
Mirror Mechanical Q	100		
Coil Current at Max. Rotation	20mA		65mA
Mirror Reflectivity	95%		
Position Sensor Linearity			0.5°

Table 2.1: Summary of TI TALP1000b MEMS mirror specifications [11]

2.1.1 Drive Hardware

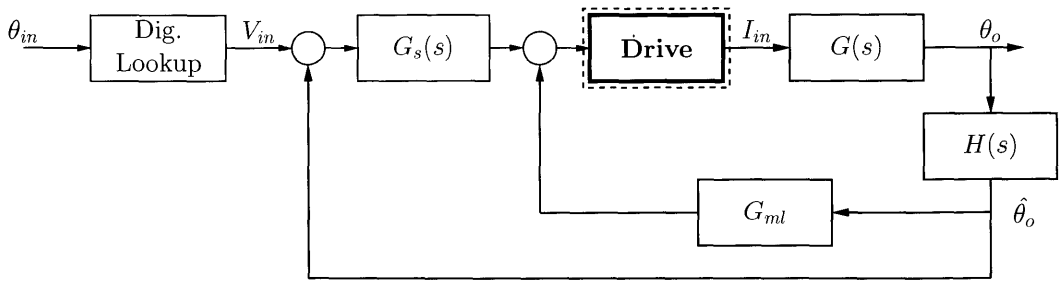

Figure 2.4: Drive amplifier block within the control system

The drive hardware for the mirror must be able to supply up to 65mA with high precision and low distortion through roughly 2kHz, the expected close-loop bandwidth of the compensated system. In general, an inductive load can be driven through either voltage or current mode control. Voltage mode control manages the voltage over the coil. The voltage is converted into a current and filtered by the impedance of the coil. In current mode control, the coil can still be driven by a voltage but the current through the coil is sensed and used as feedback to actively regulate the current through the coil. The most common way to measure current through a coil is through a small sense resistor placed in series with the coil. The voltage over the sense resistor can then be used as a feedback signal. By using feedback to control the current through the coil, the speed of the drive system is increased and DC current error due to changes in the coil impedance with temperature are removed. For these reasons, current control is generally preferred over voltage control for these applications.

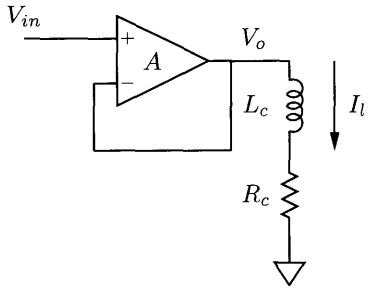

Figure 2.5: Voltage control topology

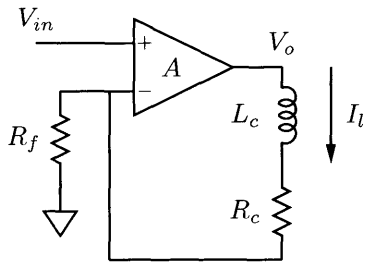

Figure 2.6: Current control topology

Considering the voltage control topology shown in Figure 2.5, the transfer function between the current through the inductor, I_l, and the input voltage V_{in} is given by Equation (2.1). In this case, the DC gain A of the amplifier is considered infinite such that $V_o = V_{in}$. The current through the inductor is filtered by the low-pass filter comprised of the series inductance L_c and resistance R_c of

the coil.

$$\frac{I_l}{V_{in}} = \frac{1}{L_c s + R_c} = \frac{1}{R_c} \frac{1}{\frac{L_c}{R_c} s + 1} \tag{2.1}$$

The current control topology shown in Figure 2.6 can be described by the block diagram shown in Figure 2.7 without the minor-loop feedback in place. The transfer function between I_l and V_{in} is given by Equation (2.2). The current control topology has the effect of moving the inductive pole out by roughly a factor of A compared to the voltage control topology. This enables the current through the coil to be much more responsive to changes in V_{in}.

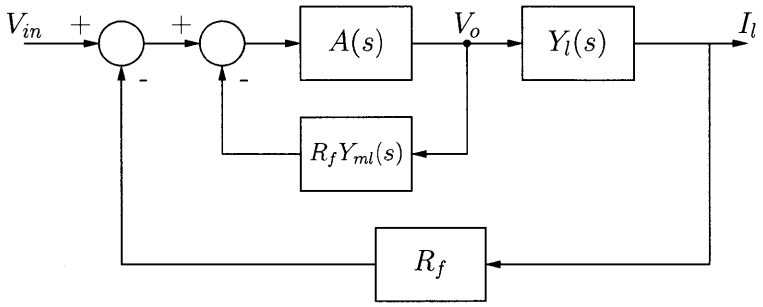

Figure 2.7: Block diagram of the current amplifier circuit with minor loop external compensation

$$\frac{I_l}{V_{in}} = \frac{A(\frac{1}{L_c s + R_c + R_f})}{1 + \frac{AR_f}{L_c s + R_c + R_f}} \approx \frac{1}{R_f}(\frac{1}{\frac{L_c s}{AR_f} + 1}) \tag{2.2}$$

Initial drive designs focused on simplicity and effectiveness. The design shown in Figure 2.8 utilizes the OPA551, a unity gain stable high output op-amp. R_f is used to set the input voltage to output current gain. With R_f =10Ω, the voltage to current gain is 100mA per volt. The zener diode pair limits the voltage drop over the drive coil to one zener voltage plus a diode drop. Careful attention had to be given to choosing the breakdown voltage of the zener diodes. Zener diodes will begin to conduct current at biasing voltages below their zener voltage, creating a rounded knee in the voltage to current relationship instead of a sharp corner. If the zener diodes shown in Figure 2.8 steal too much current from the drive coils while the mirror is within proper angular ranges, the mirror can begin to oscillate. Therefore, the zener voltages were chosen to provide linear operation out to 4.5V (the maximum voltage over the voice coils). A pair of 500mW 6V zener diodes accomplishes this task.

Driving a series inductance and resistance under current control causes similar problems to driving a capacitive load under voltage control. This can be seen by considering the transmission of the

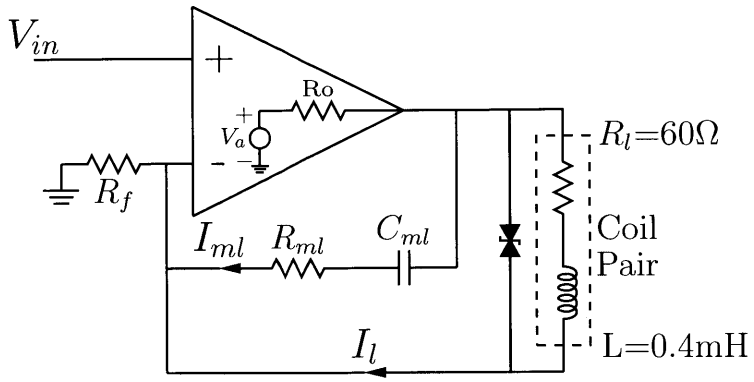

Figure 2.8: OPA551 Current amplifier circuit with external RC minor-loop compensation

inductive feedback loop, given by Equation (2.3). The inductance and resistance create an additional pole in the uncompensated loop transfer function. If the pole is far enough below the crossover frequency of the op-amp, the decrease in phase margin can potentially cause the system to become unstable or, in the very least, can cause undesired ringing at the new crossover frequency.

$$Y_l(s) = \frac{I_l}{V_a} = \frac{1}{R_o + R_l + R_f + Ls} \tag{2.3}$$

The specifications for the OPA551 list an open-loop crossover frequency of 3MHz with a phase of 45°. The DC loop attenuation, α is given by Equation (2.4) shown below.

$$\alpha = \frac{R_f}{R_f + R_o + R_l} \tag{2.4}$$

The specifications due not provide any information regarding the output impedance, R_o, of the OPA551. However, given a step input signal, the output current will ring with a frequency that is roughly equal to the crossover frequency of the attenuated loop frequency response. As shown in Figure 2.9, the uncompensated step response rings with a frequency of roughly 81kHz. Using the peak overshoot of the step response, the attenuated loop response has an approximate phase margin of 21.54°. Finally, given that the two poles of the amplifier are located at 1Hz and 3MHz, the pole caused by the inductance and resistance of the loop must be located at roughly 35kHz, resulting in an R_o of 18Ω and a loop attenuation of 19dB as shown by Equation (2.5).

$$\alpha = \frac{R_f}{R_f + R_o + R_l} = \frac{10}{10 + 18 + 60} = 0.113 \approx -19dB \tag{2.5}$$

Using a minor loop feedback approach, the transfer function can be altered to compensate the

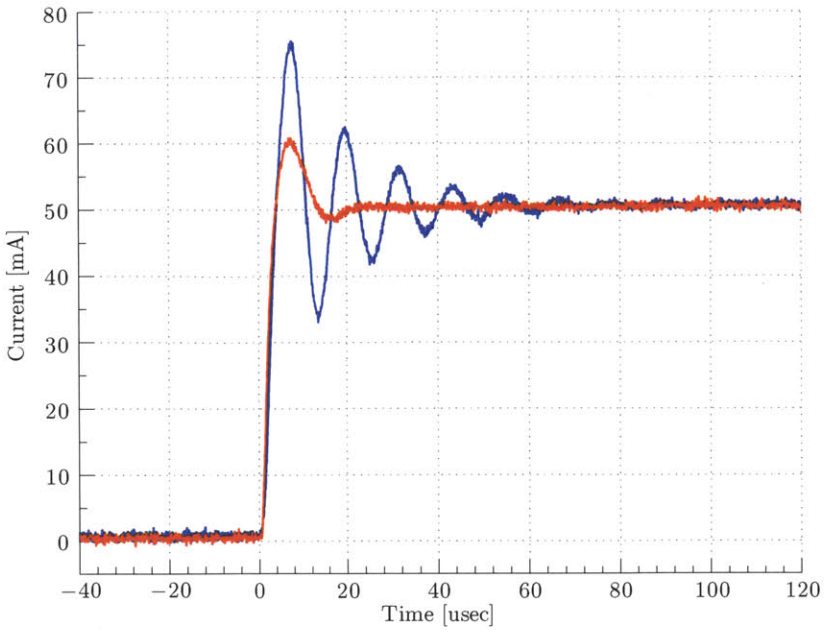

Figure 2.9: Comparison of the uncompensated and compensated step responses

inductive pole [13]. Figure 2.7 shows a block diagram with the op-amp transfer function, $A(s)$, the transmission transfer function of the voice coils, $Y_l(s)$, and the minor-loop feedback network, $Y_{ml}(s)$.

The minor loop feedback network must contain a pole at the same frequency as the pole generated by the coil. The minor loop pole then becomes a zero in the closed loop op-amp transfer function to effectively cancel the dynamics of the inductive coil. Since the drive circuit uses current feedback, the admittance of the compensation network is considered. As shown in Figure 2.8, a series resistor capacitor network accomplishes this task with the transfer function shown by Equation (2.6).

$$Y_{ml}(s) = \frac{I_{ml}}{V_o} = \frac{C_{ml}s}{R_{ml}C_{ml}s + 1} \tag{2.6}$$

Choosing an R_{ml} of 430Ω and a C_{ml} of 10nF, the compensated open loop crossover frequency is 102kHz, slightly lower than the uncompensated crossover frequency. However, the phase margin has increased to 52°, providing a much more stable response. Figure 2.9 shows that the minor-loop has created a system with comparable speed but much less overshoot and ringing. Likewise, Figure 2.10 shows a simulation of a comparison between the compensated and uncompensated open-loop frequency responeses. The compensated loop response shows a comparable crossover frequency but much higher phase margin.

The drive circuit operates with an efficiency that can be approximated by the maximum voltage

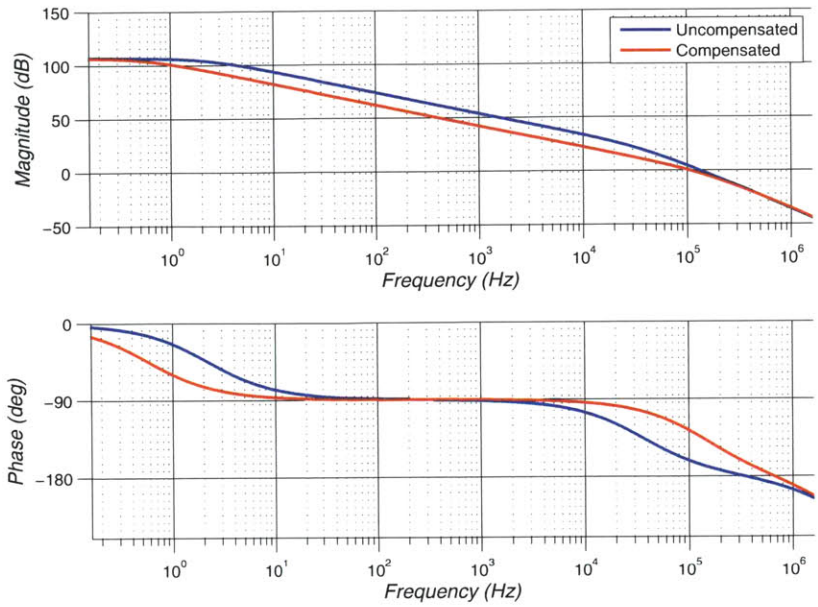

Figure 2.10: Comparison of the uncompensated and compensated drive amplifier frequency response

applied over the load coil, $V_{o,max}$, divided by the source voltage, 24V. At full angular rotation, $V_{o,max} \approx 5V$, resulting in an ideal efficiency of roughly 21%.

2.1.2 Position Feedback

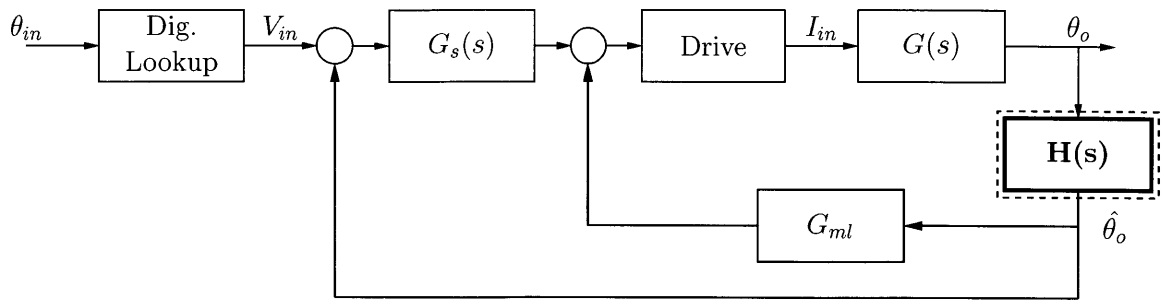

Figure 2.11: Internal position feedback block within the control system

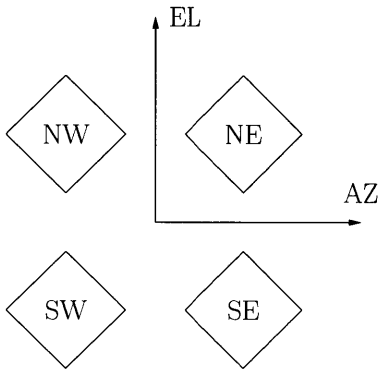

Figure 2.12: Orientation and position of the quadrant cell array

Each quadrant of the quad cell, represented in Figure 2.12, is operated in photo-voltaic mode giving a voltage that is proportional to the intensity of light incident on the cell. Equations (2.7) and (2.8) are used to convert the four voltages into an azimuth and elevation estimation.

$$AZ = \frac{(NE + SE) - (NW + SW)}{NW + NE + SW + SE} \tag{2.7}$$

$$EL = \frac{(NE + NW) - (SE + SW)}{NW + NE + SW + SE} \tag{2.8}$$

Simply put, azimuth is estimated as the normalized east and west difference while elevation is estimated as the normalized north and south difference. Since each quadrant output is directly proportional to the amount and intensity of incident light, the azimuth and elevation estimations represent the centroid of the laser spot location, even if the spot is non-circular. However, quad cells suffer from nonlinearity around the edges of operations, as will be discussed in Chapter 4.

In order to implement Equations (2.7) and (2.8) in hardware, an analog division is required.

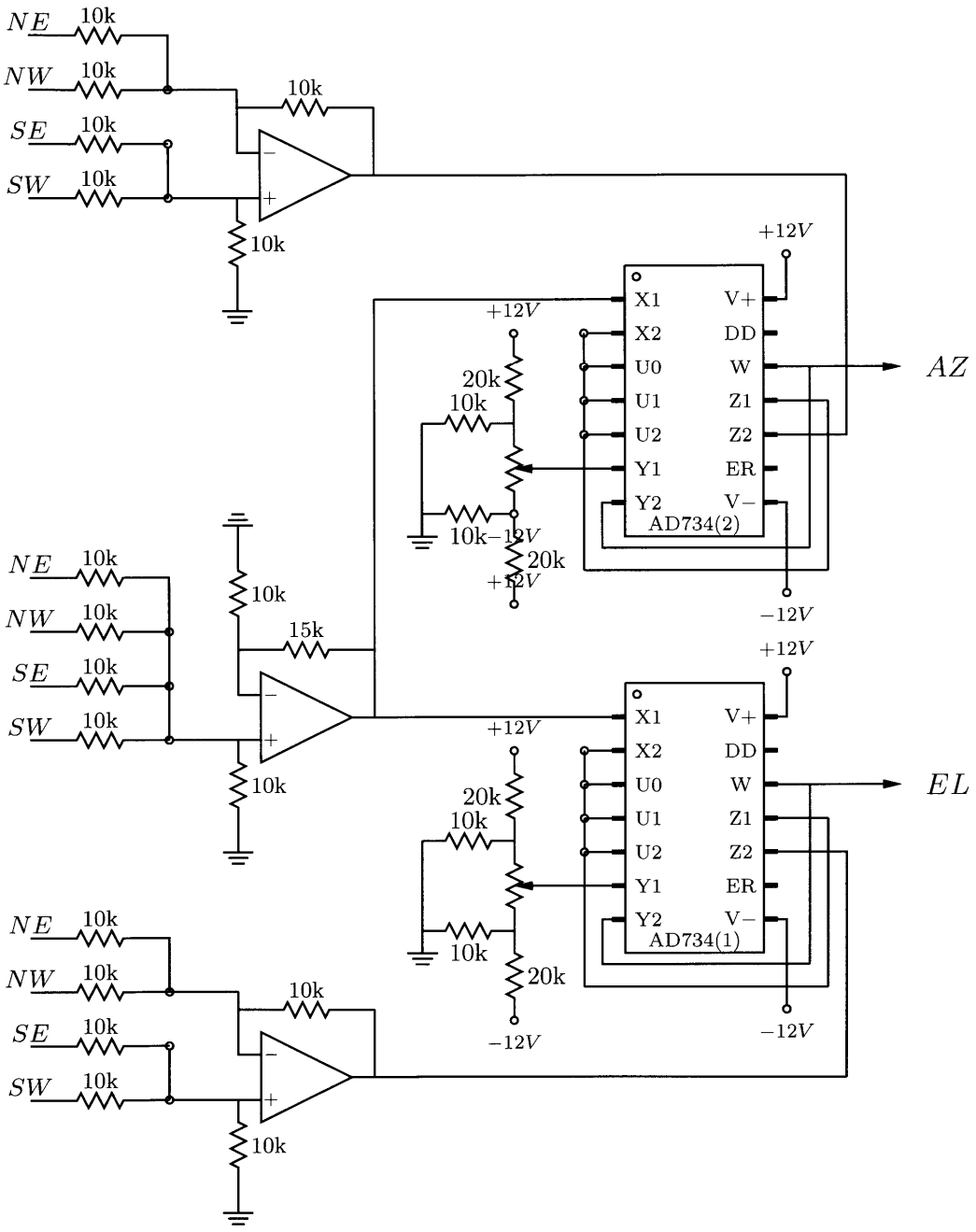

Figure 2.13: Quadcell hardware

Analog division can be performed using standard op-amps through the use of log and anti-log circuits. However, for this design, the AD734 analog multiplier divider was utilized. The AD734 can implement a variety of different transfer functions depending on the configuration used. The transfer function implemented in this design is given by Equation (2.9).

$$W = U\frac{Z_2 - Z_1}{X_1 - X_2} + Y_1 \tag{2.9}$$

Figure 2.13 shows a schematic circuit used to normalize the quad cells to produce azimuth and elevation angle estimations. Two AD734 chips are used to continuously calculate normalized azimuth and elevation angles described by Equations (2.7) and (2.8), respectively. In both cases, X_2 is set to ground and X_1 is set to the summation of each quadrant voltage. Z_2 and Z_1 are then set to the appropriate sum of either east and west or north or south voltages for calculating azimuth and elevation, respectively. The Y_1 input is connected to a potentiometer in order to provide an easily variable voltage level as the operating point to the system.

Chapter 3

Test Instrumentation

Compensation for the mirror was largely designed in the frequency domain. Conversely, sensor and mirror linearity as well as repeatability were evaluated in the spatial domain. The instrumentation to conduct frequency and spatial measurements along with surface profile measurements and the development environment are discussed in this chapter.

3.1 Frequency Measurements

A Hewlett-Packard 3562A Dynamic Signal Analyzer was used to conduct all frequency based measurements. The instrument has a bandwidth of 100kHz and a measurement range of 150dB. Additionally, accuracy for the frequency response magnitude and phase is $\pm$ 0.1dB and $\pm$ 0.5°, respectively. Given that the dominant poles and zeros of the mirror and compensation are well below 100kHz, the HP3562A provides sufficient performance for our purposes.

In conducting frequency response measurements, a swept sine wave input signal was given to the device under test (DUT). The HP3562A compares the magnitude and phase of the input(CH2) and output(CH1) signals and generates traditional magnitude and phase plots which can then be used

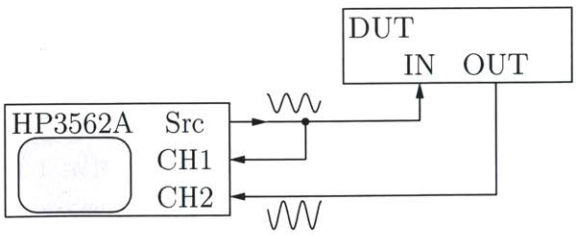

Figure 3.1: Frequency Measurement Test Bench

to analyze plant behavior and compensation design. Figure 3.1 shows the general configuration used for frequency measurements.

3.2 Spatial Measurements

While the mirror assembly includes internal position feedback, it is necessary to accurately and precisely measure the actual mirror angular position in order to properly calibrate the beam steering system. The error of the lookup table, and therefore the error of the final beam steering system, is dependent on the precision of the instrumentation used throughout calibration. Therefore, careful attention must be given to ensure that each measurement is accurate to within desired specifications.

An Aptina USB camera was used to acquire images of the laser spot directed onto a target grid. Matlab was used to process each digital image from the camera. First, the camera introduces lens distortion to each one of its images. Therefore, as discussed in section 3.2.1, an initial anti-distortion filter is applied to every image in order to remove lens distortion. In order to isolate the laser spot from the rest of the image, five background images are taken and averaged together. The image of the grid printed on the background target is then traced into Matlab to serve as a position reference. Next, with the laser turned on, an new image is taken. The average background is subtracted from each new image, resulting in an image containing the laser spot and speckled noise. This image is then used to find the centroid of the laser spot, as discussed in section 3.2.2. Finally, the location of the centroid with respect to the background grid is used to determine the exact angular position of the mirror. In order to prevent laser light from interfering with the quad cell array, a restrictive aperture and focusing lens were placed prior the mirror to focus the beam onto the center of the mirror. The test bench for these measurements is represented in Figure 3.2.

3.2.1 Removing Distortion

There are two general types of distortion common when using a standard camera, perspective distortion and lens distortion. Perspective distortion is created when the target is viewed at an angle other than the angle at which the image is evaluated. In order to remove perspective distortion from each image, the camera was carefully aligned to be orthogonal to the target. Next, lens distortion is caused by the fact that typical lenses found in camera optics are not rectilinear. In particular, the Aptina USB camera causes what is known as "barrel distortion". Barrel distortion makes the image appear as if it is being expanded. Figure 3.3(a) shows a background image prior to passing through the barrel distortion filter. The white lines represent the location of the outside grid as seen by the

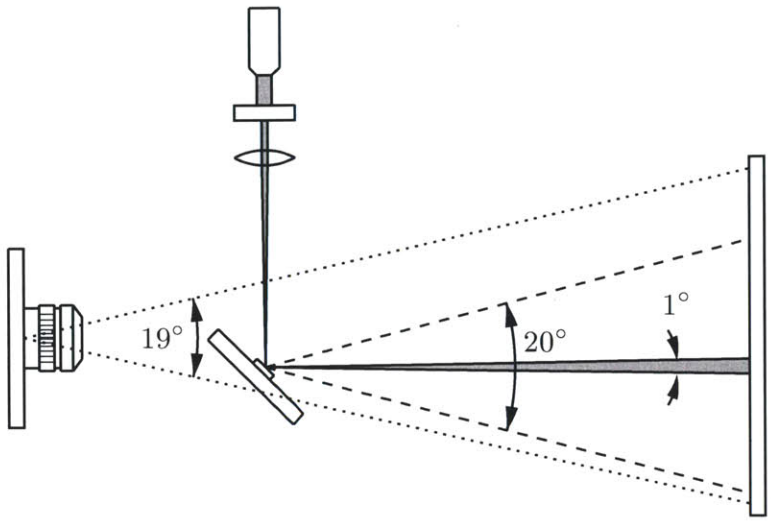

Figure 3.2: Angular measurement test bench

camera. The red lines represent a perfectly linear connection between each outside grid corner. As one can see, barrel distortion causes the grid lines to bend outward from the center. In this case, the distorted grid lines would cause a 4mrad error in the estimated position of the beam if the grid was assumed to be linear.

Barrel distortion follows the equation

$$s = r + a \cdot r^3, \quad a > 0 \tag{3.1}$$

where r is the radius to a given pixel location, a is a scaling factor that controls the degree of distortion, and s is the radius to the distorted pixel location. To correct for barrel distortion, Equation (3.1) is applied to each pixel in the image but with $a < 0$. The value of a used to remove the barrel distortion generated by the Aptina USB camera was -2.5×10^{-8}. Figure 3.3(b) shows the corrected image with significantly improved barrel distortion.

3.2.2 Finding Centroid

After removing lens distortion, the next step is to subtract the average background image, creating a difference image, and to locate the exact location of the laser spot in the difference image. The most common method of doing so is through calculating a weighted centroid.

In order for a weighted centroid algorithm to accurately determine the true center of the laser spot, the spot should exhibit uniform or at least symmetric intensity over its center. The intensity of the beam directly at the output of the laser source can be accurately modeled by a Gaussian

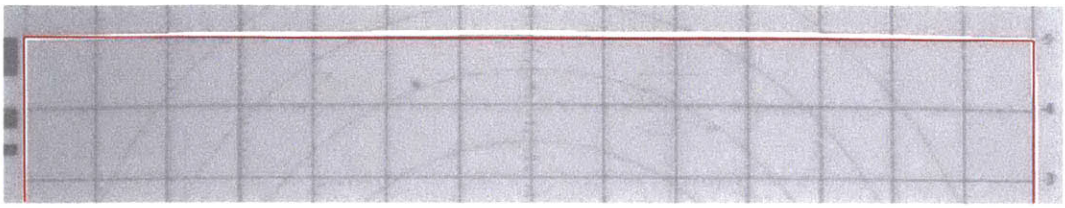

(a) Image of the background grid showing clear barrel distortion

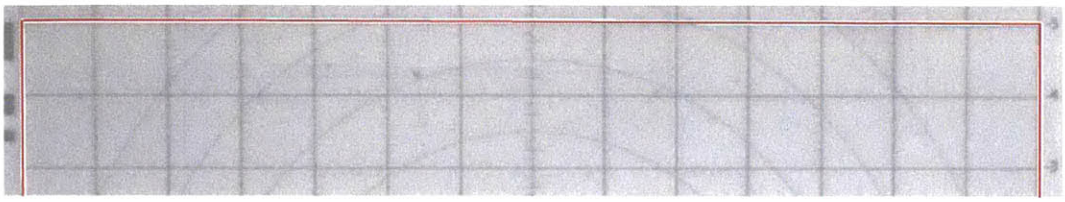

(b) Same image of the background grid after the barrel distortion algorithm was applied

Figure 3.3: Background image with and without barrel distortion

distribution. However, if Gaussian beam is incident on an aperture with a diameter that is much less than the beam diameter, the beam can be approximated by a plane wave. A plane wave incident on a circular aperture followed by a focusing lens exhibits a diffraction pattern known as an Airy Disk that can be understood using Fraunhoffer diffraction. The Airy Disk is exemplified in Figure 3.4

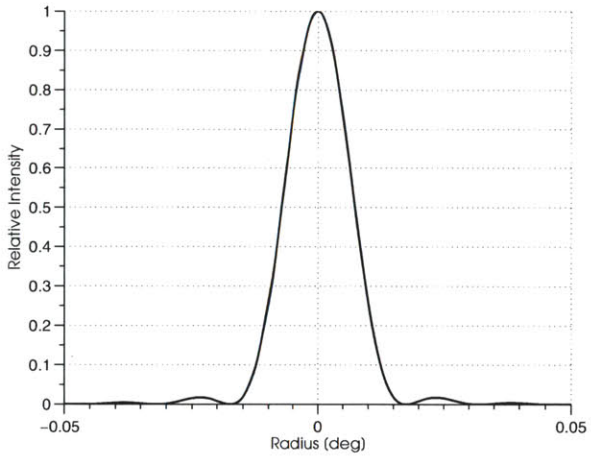

Figure 3.4: Airy diffraction pattern

Upon reflecting off of the surface of the mirror, the beam once again undergoes diffraction and takes on a pattern dependent on the angle of the mirror. Unfortunately, the camera is unable to detect such a fine deviations in intensity. The laser spot generally saturates the camera imager over the majority of the spot's area. Figure 3.5 shows the intensity profile of a cross section of the laser spot as seen by the camera.

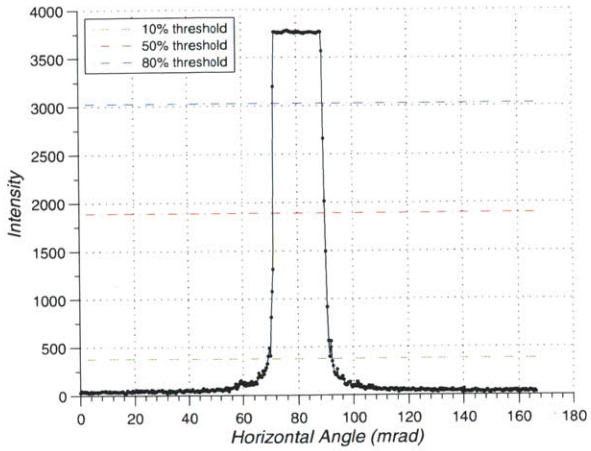

Figure 3.5: Laser spot intensity cross section

The centroid function weights each pixel by its intensity value, p, and normalizes it to the total intensity of all the pixels. The weighted centroid function is applied along both the x and y axis to achieve a two dimensional centroid. The formula for the centroid ($\bar{x}$,$\bar{y}$) given an m by n region is shown in Equation (3.2).

$$\bar{x} = \frac{\sum_{y=1}^{n}\sum_{x=1}^{m} p_{x,y}x}{\sum_{y=1}^{n}\sum_{x=1}^{m} p_{x.y}} \qquad \bar{y} = \frac{\sum_{y=1}^{n}\sum_{x=1}^{m} p_{x,y}y}{\sum_{y=1}^{n}\sum_{x=1}^{m} p_{x,y}} \tag{3.2}$$

Two primary sources of error exist when measuring the centroid location. First, changes in the room lighting could create large areas in the difference image with non-zero intensity. Depending on the location of the lights in the room, these areas may or may not be uniform over the image. While the changes in intensity may be very small, since they occupy a large area in the difference image they can sway the centroid calculations. The second source of error is caused from stray laser light being reflected off the mirror's backplane or magnets, creating non-uniform illumination outside of the beam location. While these reflections are generally small and scattered, their strong intensities can have a significant effect on the weighted centroid calculation.

In order to reduce the contribution from room lighting, an intensity threshold was implemented. Any pixels in the difference image with an intensity below the threshold were not considered in the weighted centroid calculation. However, much of the stray laser light has an intensity comparable to the laser beam intensity such that using a threshold only minimally reduces the affect of the stray laser light. Therefore, to reduce the affect of stray laser light, only the largest connected portion of the difference image was considered. Pixels are considered connected if they have non-zero values and

are adjacent to one another. Since the stray laser light is commonly fragmented over the difference image, each connected component is smaller than the laser spot and is consequently neglected during the centroid calculation.

By using an intensity threshold, a certain amount of the laser spot's perimeter is neglected. If a very high threshold is used, only a small portion of the beam spot remains. Conversely, a very low threshold would not neglect outside noise as well. The performance of the centroid algorithm therefore depends on the chosen threshold level. Figure 3.6 shows the results of the weighted centroid algorithm using three different thresholds including the results of using an unweighted centroid. Using a threshold of roughly 10% the saturation level resulted in the best performance. This threshold gives the largest laser spot while still neglecting outside noise.

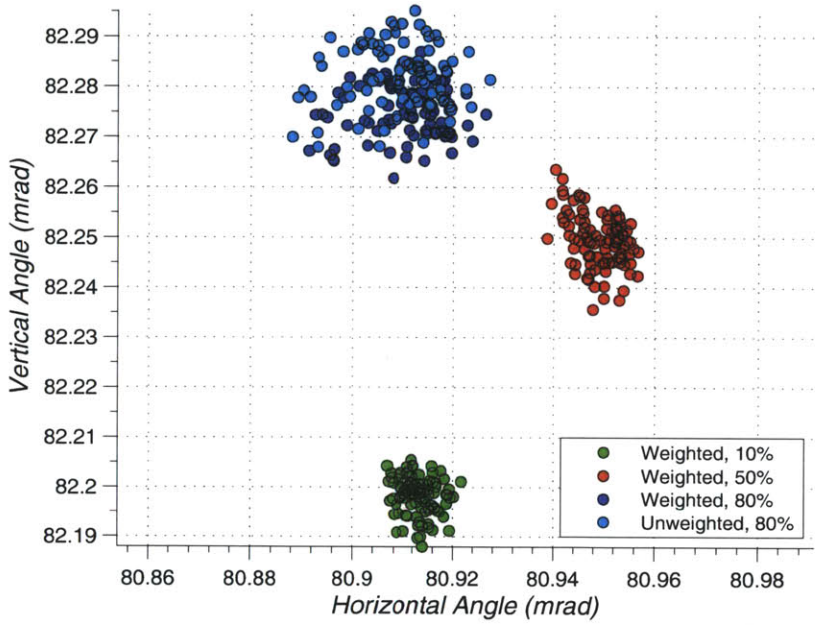

Figure 3.6: Centroid clusters under varying intensity thresholds

The fact that not all of the groups are centered around the location indicates that there is some non-uniformity to the laser spot. This non-uniformity is most likely a result of small imperfections in the alignment of the aperture and focusing lens. With the described test bench, resolution on the order of 0.05 pixels is achievable from a 1MP image, translating to 20 μrad of possible angular resolution. 20μrads of angular resolution is sufficient for our purposes, though it may be possible to achieve better centroid resolution using a higher resolution image.

3.2.3 Determining Angular Position

Once the location of the centroid is found, it can be referenced to the background grid in order to determine the angular position of the mirror. This requires that the background grid be mapped onto image coordinates within Matlab. Various algorithms to perform auto-detection of the background grid were explored that focused primarily on the detection of significant features of the background, such as the outer perimeter and intersections of the grid lines. However, none of these algorithms resulted in a mapping with sufficient robustness and precision. Therefore, after the background images have been averaged together, the background grid is mapped by hand in Matlab. This technique, while slightly more time intensive, resulted in significantly better consistency. Figure 3.7 shows an image of the background with the grid mapped onto through Matlab.

The final spatial location of the beam is estimated by calculating the horizontal and vertical distances between the centroid position surrounding grid lines. Determining the angle of the mirror follows from simple trigonometry.

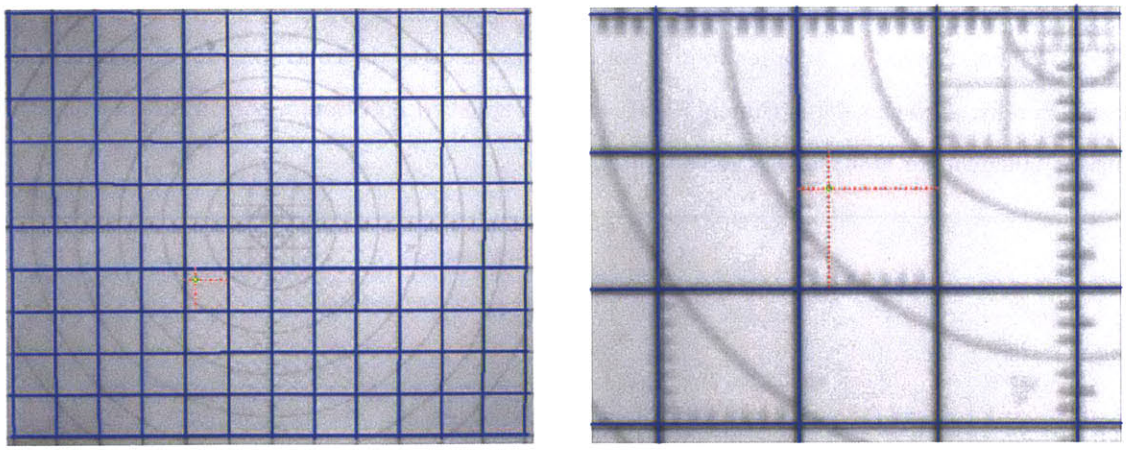

(a) Full background with mapped grid

(b) Isolation of the centroid estimation

Figure 3.7: Background image with mapped grid and centroid estimation overlayed

3.3 Surface Profile Measurements

The surface profile of the mirror is an important factor in evaluating the optical performance of any beam steering system. If the surface of the mirror is very rough, an incident laser beam will scatter, dispersing its energy over a wider field of regard. In order to maintain small beam dispersion angles, a smooth mirror surface is necessary. In addition to being smooth, the surface of the mirror must

also be flat because a small radius of curvature will also cause beam dispersion.

In order to measure the RMS roughness and general shape of the mirror, a Zygo Surface Profiler was used. The Zygo Surface Profiler uses light interferometry to acquire 3-D images of a surface with less than 0.1nm vertical resolution and less than 0.01nm RMS repeatability error [15].

3.4 Development Environment

A number of different development platforms were used in order to interact with the mirror and compensation hardware. Initial development was performed using a Cypress Semiconductor Programmable System on Chip that included a 32-bit ARM microprocessor. In order to facilitate adding digital components to the controller and beam steering platform, later development was moved onto a Xilinx Spartan-6 FPGA. Each platform was connected to a computer via a serial command line. Running either through a terminal or Matlab, serial commands are sent to the development board which then process the commands and perform the desired actions. In order to transmit and receive serial data on the Xilinx FPGA, a μBlaze microprocessor core was generated and included in the digital design. The primary function of the development hardware was to provide data to two digital-to-analog converters in order to give voltage commands to the controllers for each axis of the mirror. Finally, a National Instruments USB DAQ coupled to LabView was utilized for collecting transient behavior for analysis on the computer.

Chapter 4

MEMS Mirror Characterization

A series of electro-mechanical and optical tests were conducted in order to properly understand the potential capabilities of the mirror system. The electro-mechanical testing would indicate what type of control system should be implemented and the kind of performance specifications that can be achieved. Likewise, optical testing would indicate the types of systems the mirror is suitable for, be it 100km optical communication or close range imaging.

4.1 Electro-Mechanical

4.1.1 Linearity

Many of the analytical tools utilized throughout control and electrical engineering rely on linear transfer functions. Unfortunately, nonlinearities are inevitable and, depending on their magnitude, can make control design increasingly complex.

There are two dominant systems in the mirror whose nonlinearities can have an affect on pointing performance; the drive system and position sensor network. Nonlinearities in the drive system and position sensor network can ultimately alter the loop gains of a control system, potentially diminishing dynamic performance, and may create the need for a digital look-up table to achieve accurate pointing. In order to measure the linearity of each of these systems, the mirror was scanned over its range of angles while the four quad cell voltage outputs, the linearized azimuth and elevation values, and the actual angle of the mirror were measured.

The first test consisted of providing an input drive current that was incremented by roughly 4mA per step, scanning along the north-south axis while moving from east to west. The mirror was scanned from an optical angle of roughly $\pm 9^\circ$ on the horizontal axis and $\pm 7^\circ$ on the vertical axis.

The mirror hits its mechanical stops beyond $\pm 10°$ optical.

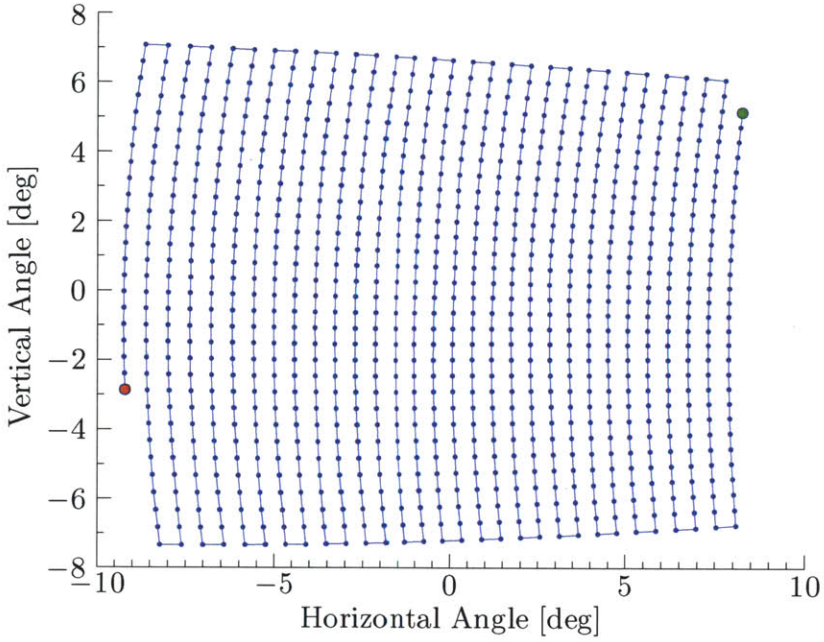

Figure 4.1: Drive linearity measurement

Figure 4.1 shows the resulting angular position measurements where each point on the chart represents one measurement. The upper-right green marker represents the first test point while the lower-left red marker represents the last measurement in the test. As can be seen from the trace, the current to position relationship in the drive system is fairly linear, that is, the equal sized steps in current resulted in roughly equal sized steps in position over the full range of angles. This is particularly advantageous if the mirror was being operated open-loop, neglecting the internal position sensors. In that case, a simple mapping function could be used to drive the mirror to desired angles. If the internal position sensors are also fairly linear then the mirror can be well controlled over its entire angular operating range. However, due to the small dampening and relatively slow response of the mirror, quick transients movements would not be feasible in open-loop operation.

Had the axes been perfectly linear and decoupled, the trace would resemble an orthogonal grid. The deviations away from a perfect grid are due to coupling between the horizontal and vertical axes. As the vertical angle increases away from $0°$, the horizontal axis tends toward positive angles, creating a gentle saddle shape along the entire horizontal scan. Similarly, as the horizontal axis moves toward more positive angles, the vertical angle tends toward the center. This effect is more prominent at larger vertical displacements.

Figure 4.2 shows the internal position feedback (IPF) values measured from the quad cell. Once

again, the green marker in the lower-left quadrant represents the beginning of the test and the red marker in the upper-right quadrant represents the last measurement in the test. With these markers, it is simple to see that the IPF measurements and angular movement are inverted to one another. Two different traces are analyzed here. The trace is the output from the analog quad cell normalization hardware. The green was generated by recording each of the four outputs from the quad cell and normalizing the values on the computer using Equations (2.7) and (2.8). Therefore, the green trace represents the digital normalization of the quad cell voltages and the blue trace represents the equivalent analog normalization. Both the analog and digital normalization closely match over the full range of angles.

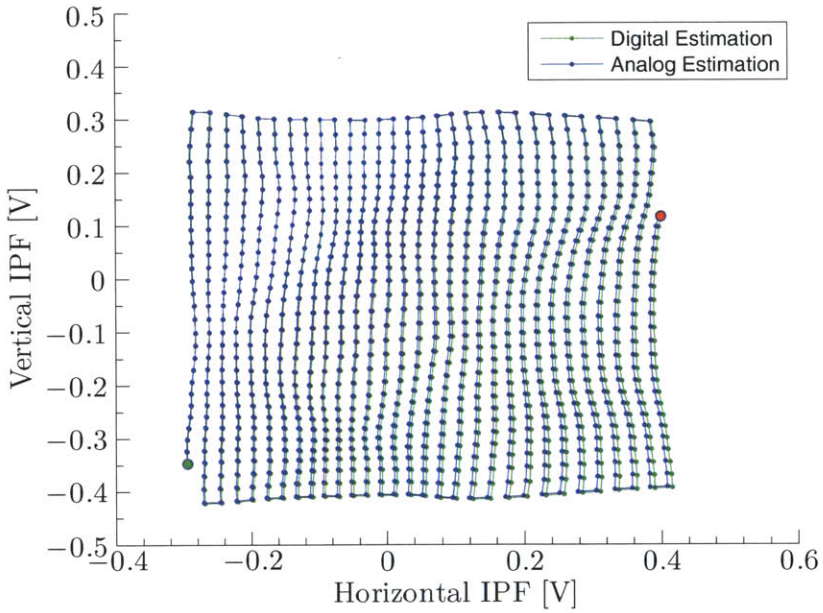

Figure 4.2: Internal Position Feedback Linearity

As expected, there is considerable nonlinearity in the internal position feedback estimation. Furthermore, at first glance, there is no clear shape to the nonlinearity that a fairly simple mapping function may be able to describe. Without a mapping function, a lookup table will have to be generated in order to accurately steer the mirror to desired angles.

4.1.2 Dynamic Response

The horizontal and vertical axis of the mirror are connected to their outer structure via two small silicon torsion connections. The dynamics of the mirror can therefore be accurately modeled by a torsional spring, mass, and damper system. The general transfer function for such a system is shown

in Equation (4.1) where ω_n is the natural frequency of the system and ζ is the damping ratio.

$$G(s) = \frac{1}{\frac{1}{\omega_n}s^2 + \frac{2\zeta}{\omega_n}s + 1} \tag{4.1}$$

Both a transient analysis and frequency analysis were performed in order to characterize the dynamic behavior of the mirror. The transient analysis consisted of measuring the angular position of the mirror to an input step in current. The angular position of the mirror was measured by recording the normalized IPF voltages. As shown in section 4.1.1, the IPF measurements contain nonlinearities that do not accurately represent the true position of the mirror. In order to minimize the affect of these nonlinearities, the step angles were performed on a single axis over small angles. Figure 4.3 shows a modeled step response of the mirror that clearly shows the magnitude of the ringing. Figure 4.4 shows a close up view of a measured step response for the horizontal axis.

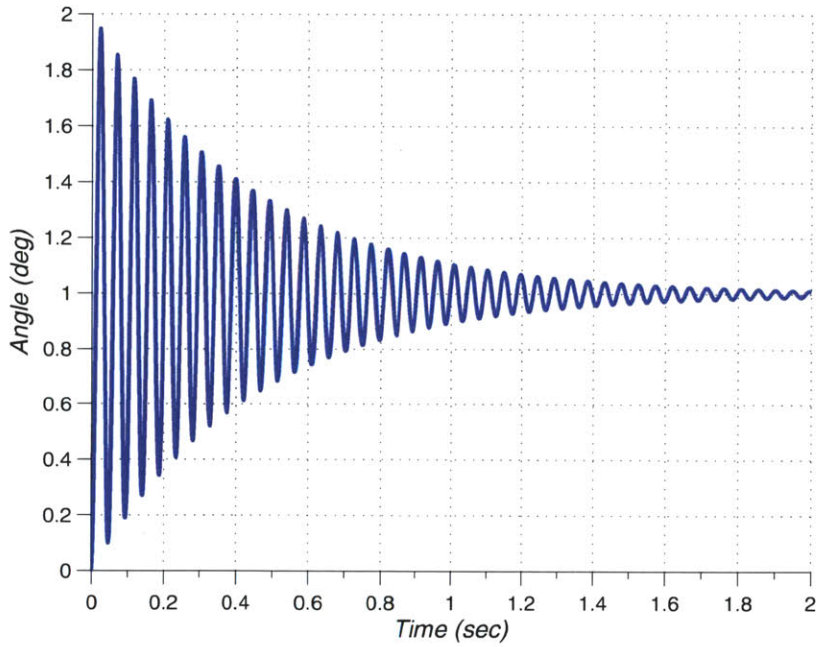

Figure 4.3: Modeled step response

The peak overshoot P_o of the step response is fully characterized by the damping ratio and is given by the Equation (4.2) where the value of P_o has been normalized to a unit step.

$$P_o = 1 + e^{\frac{-\pi\zeta}{\sqrt{1-\zeta^2}}} \tag{4.2}$$

Solving for the damping ratio results in Equation (4.3).

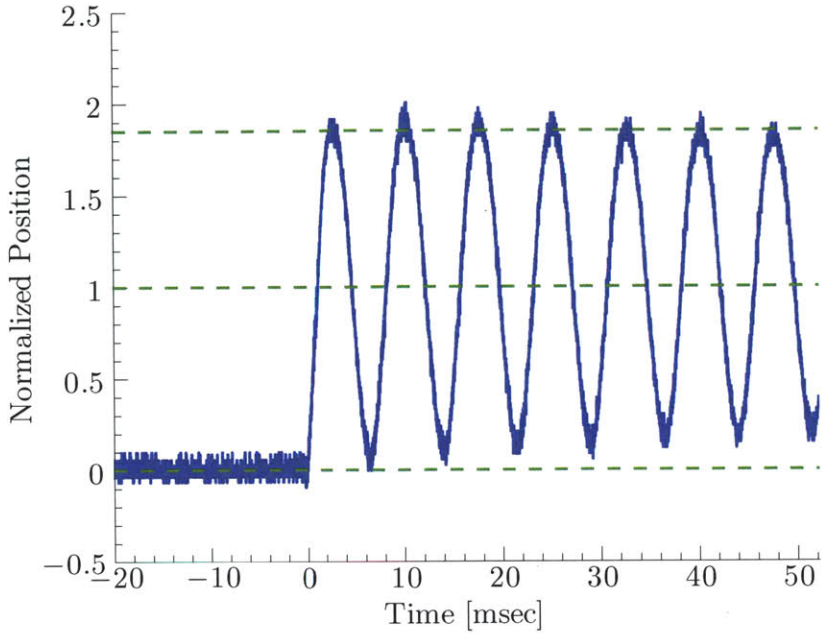

Figure 4.4: Measured step response of the horizontal axis

$$\zeta = \frac{\ln^2(P_o - 1)}{\ln^2(P_o - 1) + \pi^2} \tag{4.3}$$

The step response shown in Figure 4.4 has a normalized peak overshoot of 1.94, resulting in an estimated damping ratio of 0.017. The natural frequency, ω_n, is given by Equation (4.4) where ω_d is the measured frequency of oscillation of the step response. Since the damping ratio is so small, the natural frequency is simply approximated by the oscillation frequency.

$$\omega_n = \frac{\omega_d}{\sqrt{1 - \zeta^2}} \approx \omega_d \tag{4.4}$$

Here, w_n is measured as 134Hz. From the step response, it is clear that the mirror must be operated within a feedback loop since any small disturbance can cause significant and extremely underdamped ringing in position.

The HP 3562A Dynamic Signal Analyzer was used to generate a frequency response for each axis of the mirror. The step response has already indicated that the system is very underdamped with a natural frequency of 134Hz. The frequency response will indicate at what frequencies to provide compensation.

The source of the signal analyzer was connected to the input of the amplifier driving the axis to be evaluated. The poles of the closed-loop amplifier begin to occur around 100 kHz, far above the

dominant poles of the mirror, and should not interfere with the frequency response of the mirror. The first channel was connected to the input signal of the amplifier while the second channel was connected to the normalized IPF voltage. A logarithmic swept sine measurement was then performed from 1Hz to 100kHz. From 1Hz to 100Hz, a source magnitude of 100mV was chosen, resulting in a 10mA current magnitude through the drive coils. In order to avoid damage to the mirror around the 134Hz peaking frequency, the source magnitude was dropped to 20mV from 100Hz to 1kHz, resulting in a current magnitude of roughly 2mA. Finally, to maximize signal-to-noise ratio as the magnitude response drops off at high frequencies, a source magnitude of 2V was chosen from 1kHz to 100kHz for a current magnitude of roughly 200mA.

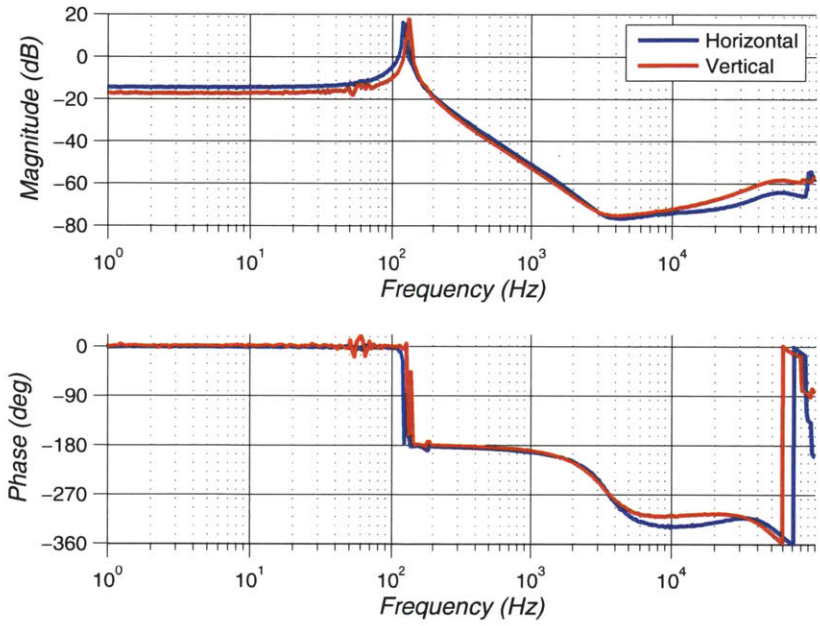

Figure 4.5: Uncompensated frequency response

The results of the measurement are shown in Figure 4.4. The horizontal and vertical axes show very similar frequency responses. Both produce a resonant peak of roughly 30dB. The magnitude peaking in the frequency response is also determined by the damping ratio, shown in Equation (4.5). Given an M_p of 30dB, the damping ratio equates to 0.0167, very nearly the 0.017 estimated by the peak overshoot in the step response.

$$M_p = \frac{1}{2\zeta\sqrt{1-\zeta^2}} \tag{4.5}$$

The vertical axis shows a resonant peak at 134Hz and the horizontal axis shows the same resonant peak at 130Hz, matching well with the observed oscillation frequency in the step response. After

the resonant peak, the magnitude drops off at 40dB per decade until approximately 4kHz when the magnitude begins to increase at roughly 20dB per decade while the phase drops by almost 180°. The increasing magnitude and dropping phase is indicative of a zero in the right half plane.

Right half plane zeros are inherently difficult to compensate for since adding right half plane poles will make the system unstable. The most effective means of compensation is to attenuate the magnitude well before the right half plane zeros occur in order to ensure stability and good gain margin. Therefore, the bandwidth of the controller will effectively be limited to below 4kHz. Using minor-loop feedback to add dampening and a lead controller to increase bandwidth, a crossover frequency of roughly 1kHz with a phase margin above 45° is achievable. Finally, the frequency response has limited DC gain and zero slope at DC. In order to improve the tracking performance of the mirror, an integration should be added to the loop. Chapter 5 further describes the compensator theory and implementation.

4.1.3 Temperature Dependence

Included on the mirror board is a small temperature sensor that can be used to measure the temperature of the board. Everything on the mirror board, including the silicon springs, the drive coils, and the photo-diodes of the quad-cell, have a behavior that is dependent on temperature.

As discussed in section 2.1, the mirror axes are attached to the outer frames via a small silicon torsion spring with dynamics that can be approximated as a second-order mass, spring, and damper system. As the temperature of the mirror changes, the spring coefficient of the linkage also changes resulting in a varying natural frequency and damping ratio. The specification sheet for the mirror indicates that the resonant frequency of the mirror, which is independent of the drive coils and quad-cell, varies 10Hz from -10°C to 70°C.

Each of the four drive coils is made of copper wire that has a resistance that is dependent on temperature. The resistance of a wire with length L, cross-sectional area A, and resistivity ρ is given by Equation (4.6).

$$R = \frac{\rho L}{A} \tag{4.6}$$

The resistivity of copper wire is measured at 1.68 $\times 10^{-8}$ Ωm with a temperature coefficient of 0.0039 K^{-1} [14]. Therefore, if we ignore the effect that temperature has on the length and area of the wire, a change of 80°C results in a 31.2% change in resistance. Given a series resistance of the voice coils of 65Ω at room temperature, a change of 20°C will increase the resistance to 70.1Ω. A change in

the resistance of the voice coils has the effect of moving the pole caused by the series inductance and resistance. Given the compensation techniques discussed in section 2.1.1, moving the pole to higher frequencies results in a slight increase in the phase margin of the current amplifier. Conversely, if the temperature of the mirror drops to 20° below room temperature, the series resistance of the coils becomes 59.9Ω. The decrease in resistance has the effect of moving the pole to lower frequencies, decreasing the phase margin of the current amplifier.

The total current, I_T, through a reverse biased photo-diode can be expressed as the difference between the dark current and photo-current I_P as shown by Equation (4.7). The dark current of a photo-diode is equivalent to the reverse bias leakage current of a standard diode given a saturation current I_S while the photo-current is the current that flows through the diode as a result of incident light.

$$I_T = I_S(e^{qV_D/nkT} - 1) - I_P, \qquad V_D < 0 \tag{4.7}$$

Increasing the operating temperature of a photo-diode devices results in changes to both the photo-current and the dark current. The photo-current is affected because changes in temperature alter the responsivity of the photo-diode by shifting the absorption spectrum. The absorption spectrum of a photo-diode is defined by how likely a photon of a certain wavelength is to generate an electrical current. In general, as temperature increases, the absorption depth of the photo-diode decreases. Therefore, the photo-diode will be less responsive to shorter wavelengths of radiation and more responsive to longer wavelengths of radiation. Figure 4.6 shows the percent change in the responsiveness of a photo-diode over the absorption spectrum.

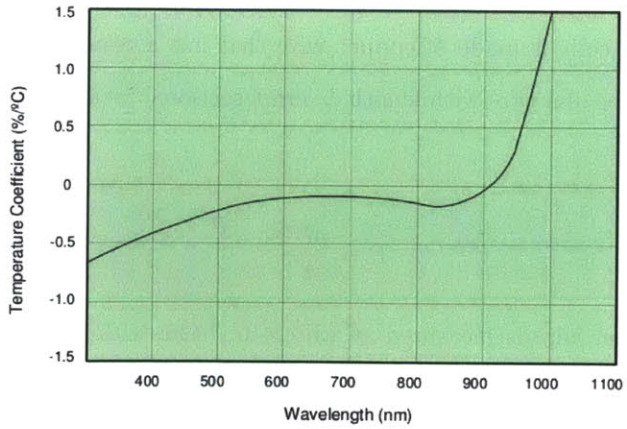

Figure 4.6: Silicon photo-diode percent change in sensitivity with varying temperature

The responsivity, R, of a silicon photo-diode as it relates to the photo-current, I_P and incident light power P is given by Equation (4.8).

$$R = \frac{I_P}{P} \tag{4.8}$$

Thus, for a given light power, the photo-current will scale with the change in responsitivity for a given wavelength. The internal LED used to illuminate the quad-cell is a red LED(700nm wavelength). As shown by Figure 4.6, the responsivity of the photo-diode at 700nm will decrease by a factor of 1.01 per degree Celcius change in temperature. Thus, as the quad-cell temperature changes, the output voltage for each quadrant will scale by a factor that is dependent on temperature. As long as each quadrant of the quad-cell remains at the same temperature as the other quadrants, the normalized beam position values given by Equations (2.7) and (2.8) will remain unchanged.

The dark current, as shown in the first term of Equation (4.7), also varies with temperature. As temperature increases the dark current increases exponentially. Therefore, if the four photo-diode quadrants vary equally with temperature, each output voltage will incur an identical offset, Δv. Thus, the denominator in Equations (2.7) and (2.8) will increase by a constant $4\Delta v$, as shown by Equations (4.9) and (4.10).

$$AZ' = \frac{(NE + SE + 2\Delta v) - (NW + SW + 2\Delta v)}{NW + NE + SW + SE + 4\Delta v} = \frac{(NE + SE) - (NW + SW)}{NW + NE + SW + SE + 4\Delta v} \tag{4.9}$$

$$EL' = \frac{(NE + NW + 2\Delta v) - (SE + SW + 2\Delta v)}{NW + NE + SW + SE + 4\Delta v} = \frac{(NE + NW) - (SE + SW)}{NW + NE + SW + SE + 4\Delta v} \tag{4.10}$$

4.2 Optical

The optical qualities of the mirror, including the mirror's surface quality and rigidity, are important in distinguishing which applications the mirror might be useful for and what steps should be taken to ensure good performance of the mirror. For instance, for long range optical communication, a surface RMS roughness of less than 10nm is preferred. However, for short range applications, such as optical multiplexers, surface roughness is not as important as switching speeds.

4.2.1 Surface Quality

It is important when designing the optical systems around the micro-mirror to understand the mirror's surface quality and shape. If the surface of the mirror is very rough, an incident beam will scatter upon contact. Additionally, if the deforms under torque, one may have to limit the range of possible drive angles or constrict the incident beam to a small point on the mirror that does not conform. A Zygo Optical Surface Profiler was used to measure the mirror's surface quality and shape.

4.2.2 Undriven

In this case, only the center region of the mirror, where the beam will be focused, needs to be smooth. The Texas Instruments documentation lists a surface RMS roughness of 200nm, which is quite poor for most applications. However, it is unclear which segments of the mirror's surface were included in this measurement.

A surface profile measurement was performed over the center 5.4 mm^2 of the mirror resulting in an RMS value of 2.4nm, much better than the 200nm listed in the documentation. Additionally, the radius of curvature of the horizontal diagonal measured roughly 171m, showing that the mirror is minimally curved while undriven. Finally, the quiescent angle of the mirror was measured to be approximately 0.8° from the back plane.

4.2.3 Driven

Performing surface profile measurements on the mirror while it is being driven to various angles confirms whether or not the mirror becomes deformed by a static drive torque. Each measurement was completed by first driving the mirror to a specific angle and measuring the radius of curvature along the axis of rotation across the center region of the mirror. The tests were performed at mechanical rotation angles of 0°, 1.25°, and 4.5° for both the azimuth and elevation axis.

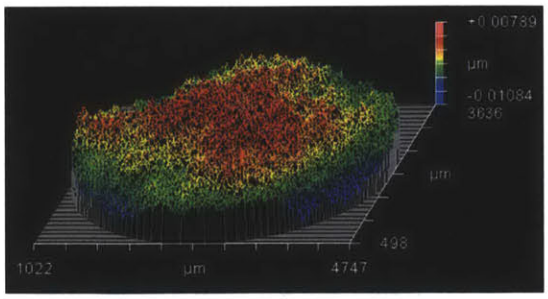

Figure 4.7: Zygo measurement of new mirror. Center 5.4mm^2 area, RMS value = 2.4nm

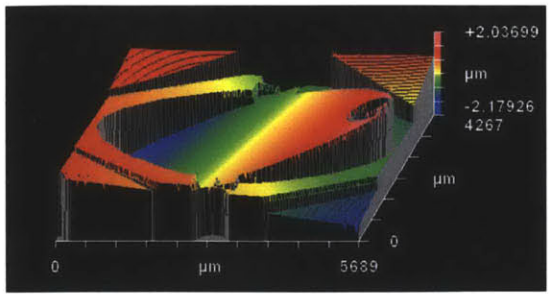

Figure 4.8: Zygo measurement showing a quiescent angle of approximately 0.08°

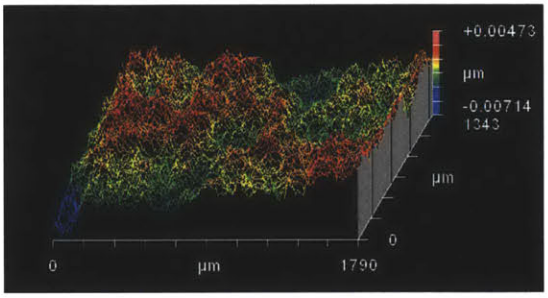

Figure 4.9: Vertical Axis deflected to 1.5 degrees

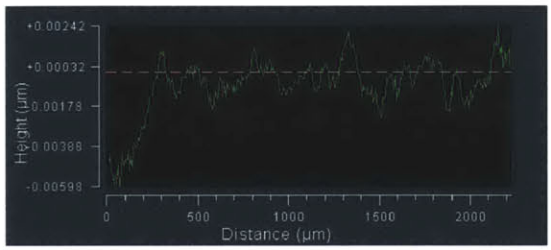

Figure 4.10: Vertical Axis deflected to 1.5 degrees

Figures 4.9 and 4.11 show a three dimensional surface profile measurement of the center 2.4mm^2 area while the mirror is being tilted to 1.5° and 4.5° mechanical rotation along the azimuth axis, respectively. At 4.5°, the mirror is nearly at the maximum rotation angle but is not contacting the physical stops that would cause additional distortion. In this case, the azimuth axis is the North-West to South-East diagonal of the three dimensional profile. Figures 4.12 and4.10 show the two dimensional cross section along this axis at 1.5° and 4.5° mechanical rotation, respectively.

At 4.5° mechanical rotation, the mirror surface becomes clearly distorted as it bends from the torque on the magnets located at the mirror's corners. At this angle, the radius of curvature measures

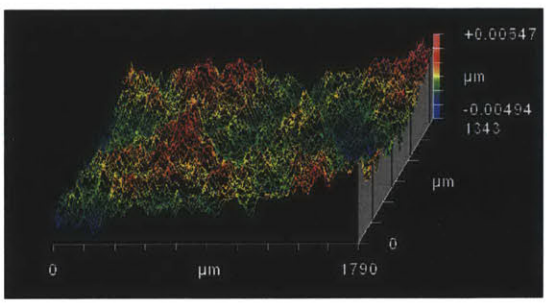

Figure 4.11: Vertical Axis deflected to 4.5 degrees

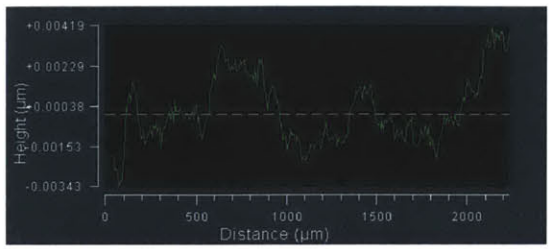

Figure 4.12: Vertical Axis deflected to 4.5 degrees

roughly 72.4m. Still, there remains a center region that is relatively undistorted. This can be more clearly visualized by Figure 4.13. The radius of curvature, R, can be approximated by the change in angle, θ, and the arc length, s, as shown by Equation (4.11).

$$R = \frac{s}{\theta} \approx \frac{670\mu m}{\frac{6.2nm}{670\mu m}} = \frac{\Delta x^2}{\Delta y} = 72.4m \tag{4.11}$$

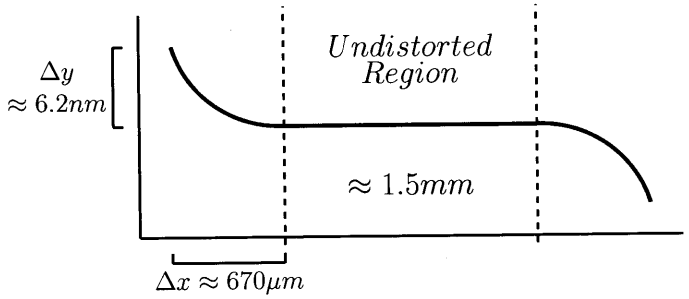

Figure 4.13: Cartoon of the mirror surface profile under static torque with 4.5° mechanical rotation

These results demonstrate the importance of restricting the laser to the center 2mm^2 region of the mirror's surface.

Chapter 5

Control

As shown by the dynamic evaluation of the mirror in Chapter 4, the sharp resonance of the mirror makes it impractical for open-loop operation. By using classical feedback techniques, the dynamic performance of the mirror can be greatly improved. This chapter describes the compensation techniques used to control the mirror.

5.1 Loop Compensation

Some of the potential applications of this fast-steering mirror include 3-D laser imaging, optical communication, and range estimation. Considering these applications, the mirror control system should be able to respond very quickly to input commands with little output error.

The ability to respond to an input command with little to no output error is directly related to the amount of gain at a given frequency in the open-loop frequency response and the number of integrations that occur in the loop. For example, ability to track fast input transitions requires large loop gain at high frequencies while zero DC error is a result of two poles located at the origin. Of course, it is essential to always maintain proper stability as well. An example of a open loop response with these traits is shown in Figure 5.1.

The infinite DC magnitude and second order roll-off at DC provides excellent tracking of input commands. Maintaining second order roll-off out until crossover will result in virtually no phase margin and consequently very poor stability. Adding a zero before the crossover frequency increases bandwidth and can result in a phase margin between 45° and 60°, ensuring fast response times and good stability.

The disadvantage of the loop response shown in Figure 5.1 is that the system is prone to oscillation

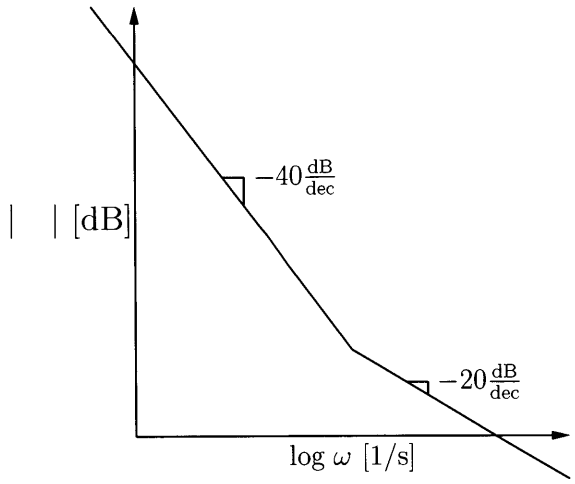

Figure 5.1: Example open-loop response for high speed and accurate tracking

if saturation occurs. Saturation will decrease the loop gain, bringing the loop magnitude response down. If the loop gain is decreased enough, the magnitude response will cross over before the phase bump from the zero occurs, resulting in very underdamped or even unstable behavior. In order to make this system robust to saturation, a more conservative loop transfer response was chosen consisting of -20dB/dec drop-off from DC to the crossover frequency. While disturbance rejection is decreased, the system will be more suitable for general purpose use.

5.1.1 Minor Loop Compensation

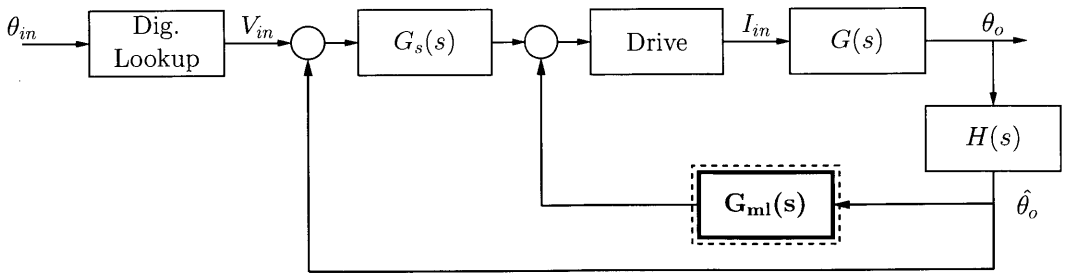

Figure 5.2: Minor-loop feedback network within control system

As shown by Figure 4.5, the uncompensated frequency response contains a very sharp resonant peak at 130Hz. This behavior corresponds to a complex pair of poles placed very far from the real-axis with a natural frequency of 130Hz. When designing compensation for this system, it is important to consider the affect of the drive electronics and sensors. In this case, the drive system contains poles at approximately 100kHz, significantly above the projected bandwidth (1kHz) of the mirror.

Additionally, the quad-cell and normalization hardware are fast enough to not contribute additional phase shift to the response of the mirror. Therefore, it is reasonable to assume that the dynamics of the drive system and position feedback network do not negatively affect the frequency response of the mirror.

The behavior of the mirror can be greatly improved through the use of feedback. The goal of the minor-loop is to effectively add dampening to the mirror. One of the simplest forms of compensation is the use negative feedback with a frequency independent gain network in the forward path, popularly known as proportional control. The effect of proportional control can be analyzed by using root-locus. The root-locus of the mirror system is shown in Figure 5.3. Here, σ represents the real axis and $j\omega$ represents the imaginary axis. As shown, applying additional loop gain to the system will only cause the poles to move farther into the imaginary plane, creating an even more underdamped system. Therefore, a slightly more complex minor-loop network is required.

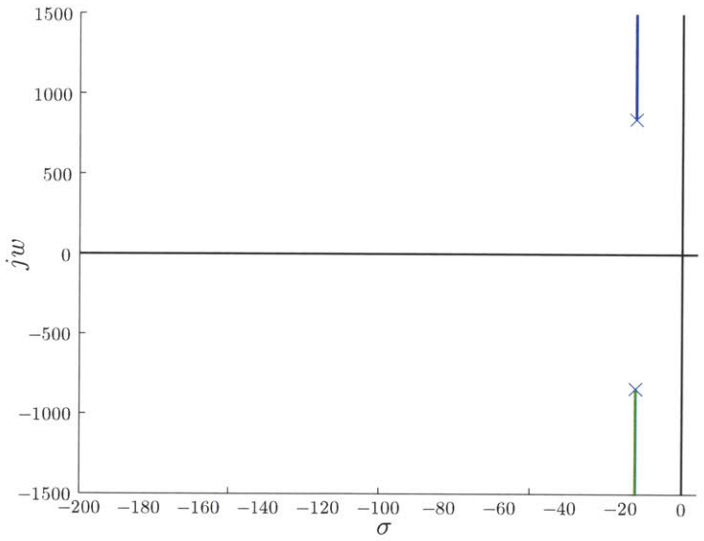

Figure 5.3: Root-locus of the mirror model

The dampening of a complex pole pair is directly related to the angle that the poles make with the real axis. Therefore, in order to increase dampening, the complex poles must be moved closer to the real axis. This is accomplished by adding a zero at the origin. A zero at the origin is effectively a differentiator. A perfect differentiator, however, has increasing gain with higher frequencies. Eventually, parasitic effects and the finite bandwidth of other op-amps would decrease the gain, still, stability and noise immunity may remain an issue. As a result, a high frequency pole is included as well. The circuit that implements this general transfer function is shown in Figure 5.4.

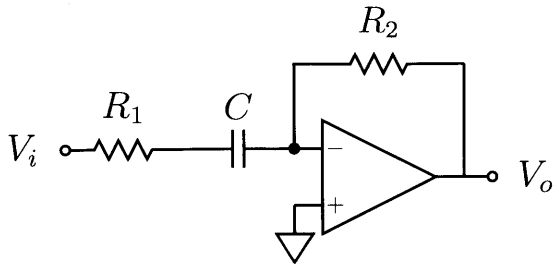

Figure 5.4: Minor-loop feedback circuit

The circuit shown in Figure 5.4 has a transfer function given by Equation (5.1).

$$G_{ml}(s) = \frac{V_o}{V_i} = \frac{-R_2Cs}{R_1Cs+1} \tag{5.1}$$

By choosing R_1 to be 10kΩ, R_2 to be 390kΩ, and C to be 0.01μ, a zero is created at the origin and a pole is placed at 10k rad/sec.

Now, as the minor loop-gain is increased, the complex poles of the mirror move toward the real axis and eventually enter the real axis at roughly 134Hz, the resonant frequency of the mechanical system. This response is shown by the root-locus in Figure 5.5. One pole heads to lower frequencies to terminate on the zero at the origin. The other pole heads toward higher frequencies to eventually break off the real axis with the high frequency pole. Therefore, by adjusting the gain of the minor loop, it is now possible to move the complex poles of the mirror to a coincident location on the real axis, effectively creating a critically damped two-pole system (while there is a third pole, it exists at high enough frequencies to be ignored when considering the primary dynamics of the mirror).

The same minor-loop method can be intuitively analyzed using Bode magnitude and phase plots. Ignoring the drive system and position feedback network $H(s)$ for now, Black's formula gives the expression of the closed-loop transfer function, shown by Equation (5.2).

$$\frac{\theta_o}{V_c}(s) = \frac{G(s)}{1+G(s)G_{ml}(s)} \tag{5.2}$$

If the loop magnitude, $|G(s)G_{ml}(s)|$, is much larger than 1, i.e. $\frac{1}{G_{ml}(s)} < G(s)$, the closed-loop transfer function can be accurately approximated by $\frac{1}{G_{ml}(s)}$. Likewise, if the magnitude of the loop is much smaller than 1, i.e. $G(s) < \frac{1}{G_{ml}(s)}$, the closed-loop transfer function can be well approximated by $G(s)$. Therefore, the closed-loop magnitude response can be approximated by taking the lesser magnitude response of $G(s)$ and $\frac{1}{G_{ml}(s)}$. Figure 5.6 shows a simulation of the magnitude response for $G(s)$ and $\frac{1}{G_{ml}(s)}$ as well as the resulting closed-loop response of the minor-loop. As can be seen,

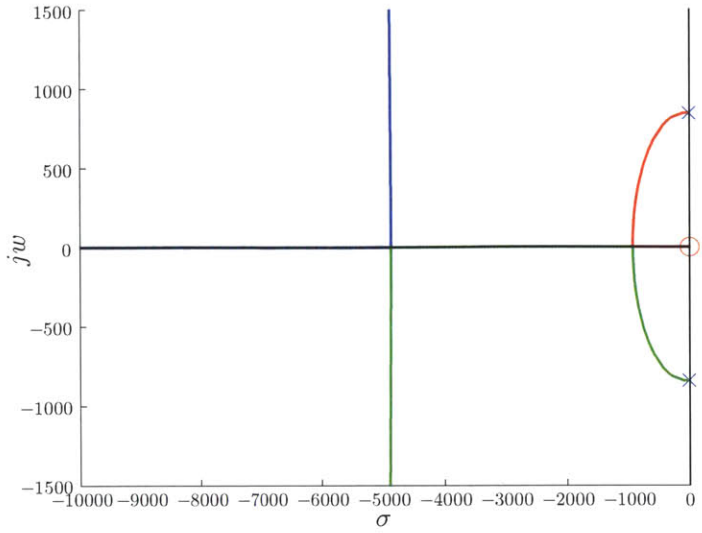

Figure 5.5: Root-locus plot of the minor loop

the closed-loop magnitude follows the smaller magnitude of $G(s)$ and $\frac{1}{G_{ml}(s)}$.

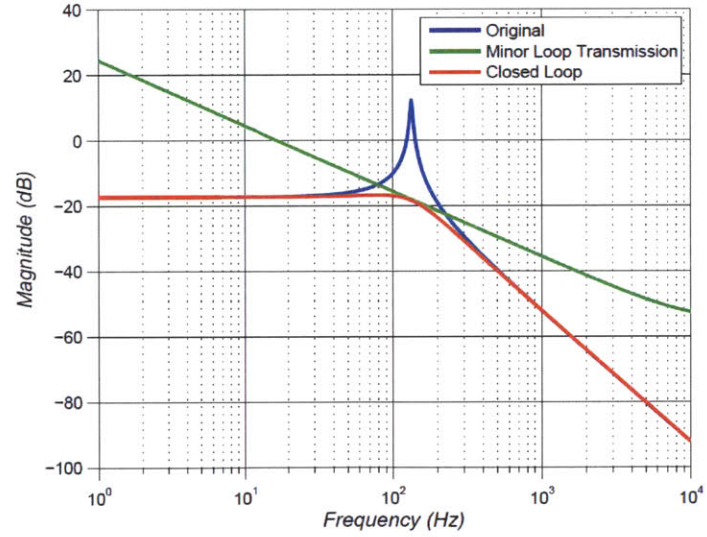

Figure 5.6: Simulated compensation design of the minor loop

By adjusting R_2 in the minor-loop feedback circuit, the DC gain of the minor can be adjusted thereby sliding the magnitude response of $\frac{1}{G_{ml}(s)}$ either up and down. The loop-gain that achieves critical damping is one that attenuates the closed-loop magnitude by 6dB at the resonant frequency.

Figure 5.7 shows a measurement of the frequency response with and without minor-loop compensation. As predicted by the simulations, the minor-loop effectively creates extra dampening without significantly affecting the bandwidth. The dampening ratio has been improved from an estimated

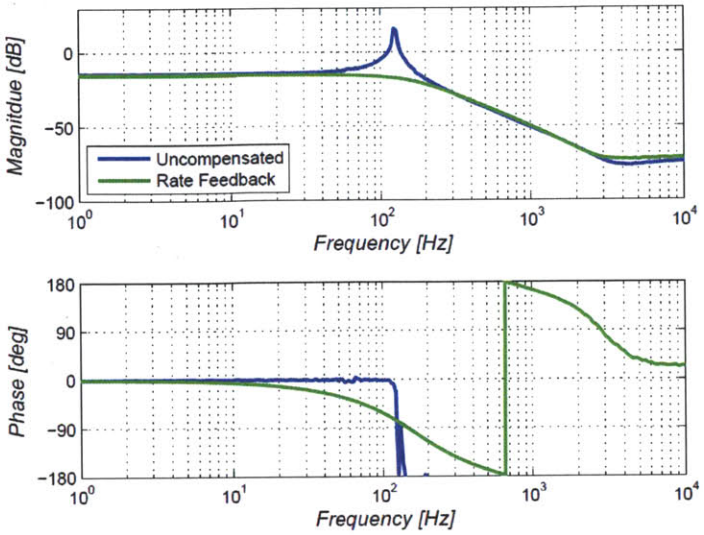

Figure 5.7: Measured frequency response before and after minor-loop feedback

0.017 to roughly 0.65. By increasing dampening, the minor-loop has created a system that is more easily controlled.

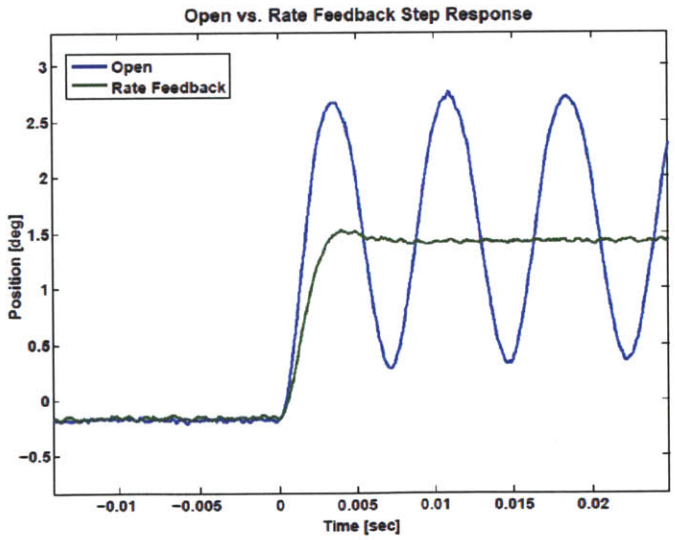

Figure 5.8: Step response with minor loop feedback

Figure 5.8 shows a measured step response of the system with and without minor-loop compensation. The rise-time of both responses are approximately equal, indicating that both systems have a bandwidth of approximately 130Hz. However, while the uncompensated step takes more than 2 seconds to settle, the compensated step response settles to 1% accuracy within 7ms.

5.1.2 Lead-Lag Compensation

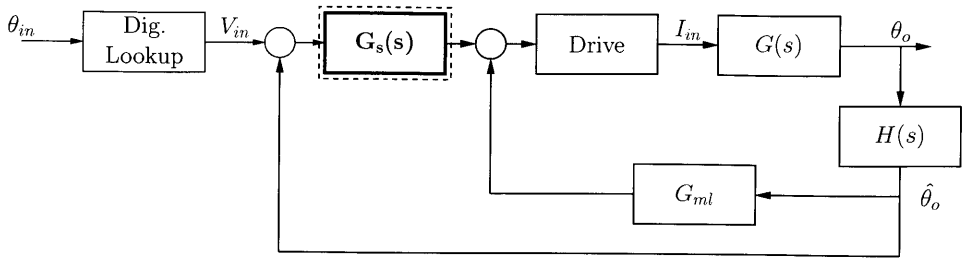

Figure 5.9: Series compensation network within control system

Minor-loop compensation created a system that is much more stable behavior than the original mirror. However, the system still exhibits poor input tracking characteristics. Specifically, the bandwidth of the system remains around 130Hz and there is non-zero steady-state error to a DC input. These problems are addressed through the use of feed-forward lead-lead compensation. The objective of lead-lag compensation is both to increase the DC gain of the loop magnitude response and to extend the unity-gain crossover frequency while maintaining good stability.

With minor-loop compensation in place, the loop response has two poles on the real axis at roughly 130Hz. In order to achieve zero offset error to a DC input, the lead-lag compensator adds a pole at the origin. With an additional pole at the origin, the loop response now has three poles before crossover and will crossover with negative phase margin, guaranteeing instability. Therefore, the two zeros of the lead-lag compensator are placed at 130Hz to effectively "cancel" the effects of the two mirror poles. Finally, the high frequency pole of the compensator is placed at 1.3kHz, ten times the frequency of the zeros.

As discussed in Section 4.1.2, the mirror response shows the presence of right-half plane zeros located roughly around 5kHz. The right-half plane zeros have the unfortunate effect of decreasing the phase margin and increasing the magnitude. This can create gain margin and stability issues if the right-half plane zeros occur close to the crossover frequency. In order to compensate the right-half plane zeros, the magnitude response must be attenuated below unity before 5kHz. By placing the lead pole at 1.3kHz, the magnitude response is attenuated well before the right-half plane zeros. Additional phase margin could be achieved by placing the high frequency pole at the a frequency higher than 1.3kHz, however, the gain margin will suffer as a result. The phase margin, Φ_m, at a crossover frequency f_c can be approximated by Equation (5.3).

$$\Phi_m = -90° - \arctan(\frac{f_c}{1.3kHz}) - \arctan(\frac{f_c}{5kHz}) \tag{5.3}$$

The pole at the origin results in an initial phase shift of 90°. Therefore, in order to maintain a phase margin of greater than 45°, the total phase shift due to the right-half plane zero and lead-pole must remain less than 45° at the crossover frequency. The phase margin at a crossover frequency of 900Hz is estimated as shown by Equation (5.4).

$$\begin{aligned}\Phi_m &= -90° - \arctan(\frac{900}{1.3kHz}) - \arctan(\frac{900}{5kHz}) \\ &= -90° - 34.7° - 10.2° \\ &= 44.9°\end{aligned} \tag{5.4}$$

Therefore, the crossover frequency must be below 900Hz in order to maintain greater than 45° of phase margin.

The circuit used to implement the discussed lead-lag compensator is shown in Figure 5.10. This op-amp circuit performs both the summation of $V_{\hat{\theta}}$ and V_{in} signals as well as the $G_s(s)$ lead-lag filter.

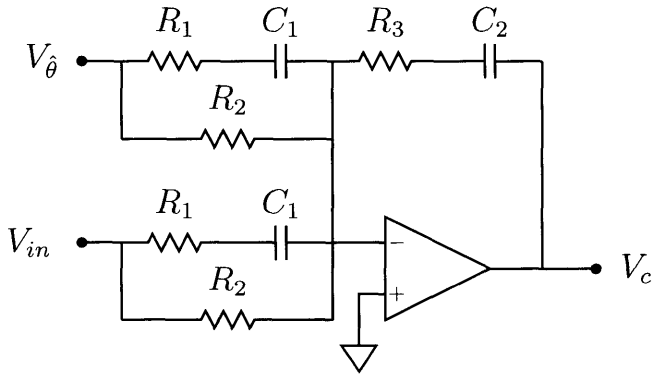

Figure 5.10: Lead-Lag series compensation circuit

The input lead network is applied to $V_{\hat{\theta}}$ and separately to V_{in}. Applying the lead filter to both $V_{\hat{\theta}}$ and V_{in} and then taking the difference of the results is equivalent to applying the lead filter once to the difference of $V_{\hat{\theta}}$ and V_{in}. This enables one op-amp to be used to implement the $G(s)$ filter and the required summation. The transfer function $G(s)$ is shown in Equation (5.5).

$$G_s(s) = \frac{V_c}{V_{\hat{\theta}}} = \frac{V_c}{V_{in}} = -\frac{(R_1 + R_2)C_1 s + 1}{(R_1 C_1 s + 1)R_2} \cdot \frac{C_2 R_3 s + 1}{C_2 s} \tag{5.5}$$

R_1	1.18k
R_2	10.7k
R_3	120k
C_1	0.1μF
C_2	0.01μF

Given the values shown above, this circuit creates two zeros, one at 133.8Hz and one at 132.6Hz, as well as a pole at the origin and at 1.34kHz. Given that the zeros of the lead-lag compensator cancel the effects of the poles at 130Hz, the magnitude response should exhibit -20dB per decade dropoff out until a crossover frequency just below 900Hz. Indeed, this is the response that was measured, as shown by Figure 5.11.

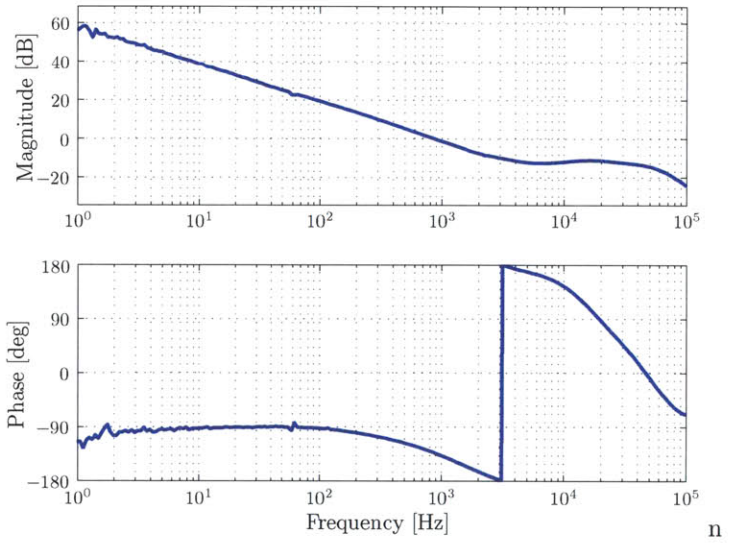

Figure 5.11: Open-loop frequency response

The open loop response shown in Figure 5.11 shows that the compensation techniques have increased the crossover frequency from roughly 130Hz to 878Hz. Additionally, the extra loop integration has created infinite DC gain and 60dB of gain at 1Hz. Finally, the resulting phase margin is measured to be 46.8°. While the right-half plane zeros slightly increase the gain above the crossover frequency, the gain margin is maintained at 10.2dB. The closed-loop frequency is shown in Figure 5.12.

As shown by Figure 5.12, the closed-loop response exhibits a flat response and slight peaking around 1kHz. The peaking in the closed-loop response is due to the 46.8° of phase margin. Taking the 3dB frequency to be after the peak, the closed-loop 3dB bandwidth is measured to be 1.9kHz.

When designing the lead-lag compensation, the expected loop response depended on a "cancellation" of the mirror poles at roughly 130Hz. Indeed, the measured loop response shows no indication

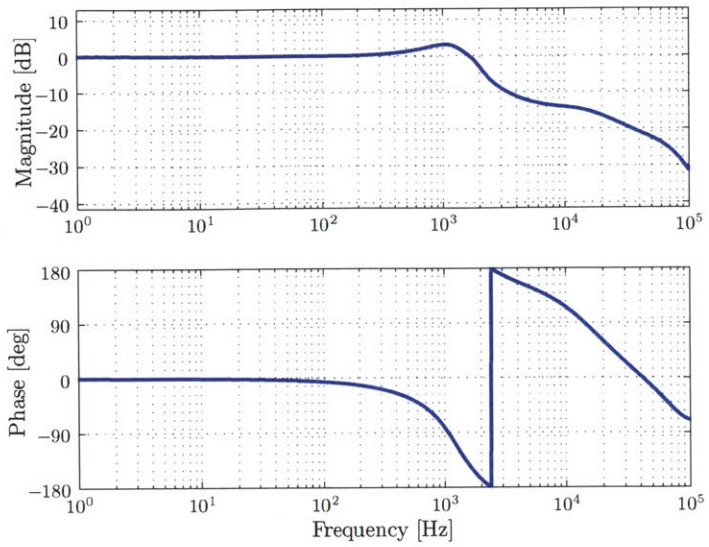

Figure 5.12: Closed-loop frequency response

of the poles. Unfortunately, the dynamics of the poles can never really be cancelled. By placing compensating zeros on top of the two mirror poles, the compensation network has created two fairly low frequency pole-zero doublets. While the effect of the pole-zero doublets is difficult to find in the loop response, it is clearly seen in the step response. Essentially, the response of the mirror poles has not been cancelled but rather made very small. The result is that the step response contains a very small exponential decay added into the response that decays with a time constant given by the inverse of the pole frequency. Since the mirror poles are well below the crossover frequency, this time constant is significantly longer than the rise time of the step response, resulting in a long transient tail. The final result is that the step response will respond very quickly to changes in the input command but will take considerably longer to settle to the final value.

The zoomed out measurement of the system's step response is shown in Figure 5.13 while a zoomed in image of the positive going step is shown in Figure 5.14. The 10% to 90% rise time is measured to be 0.798ms. The 1% settling time is measured to be 7.155ms. Finally, the peak overshoot is measured to be 12% of the step size. The full circuit of the feed-forward lead-lag compensator and coil drive is shown in Figure 5.15

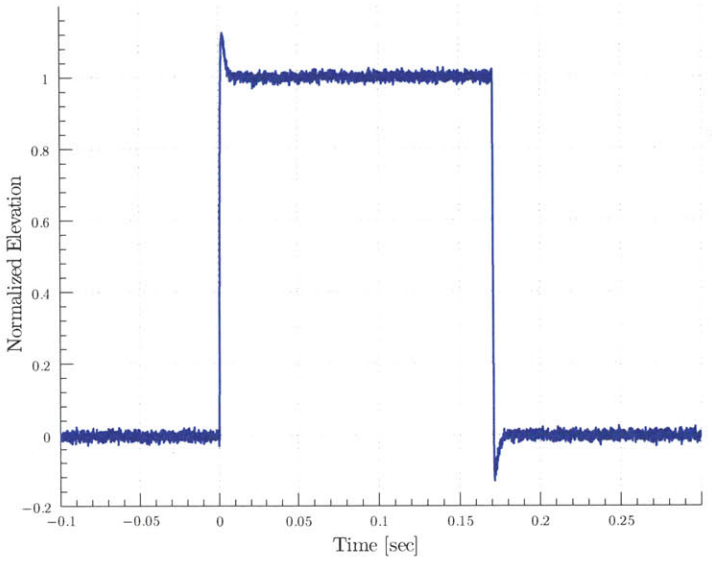

Figure 5.13: Step Response with lead-lag compensation. Measured from the internal position sensors

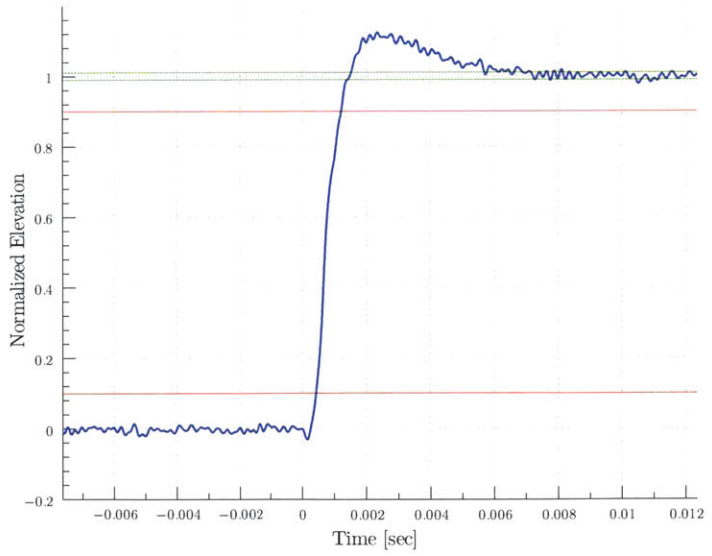

Figure 5.14: Close-up of the step response with lead-lag compensation

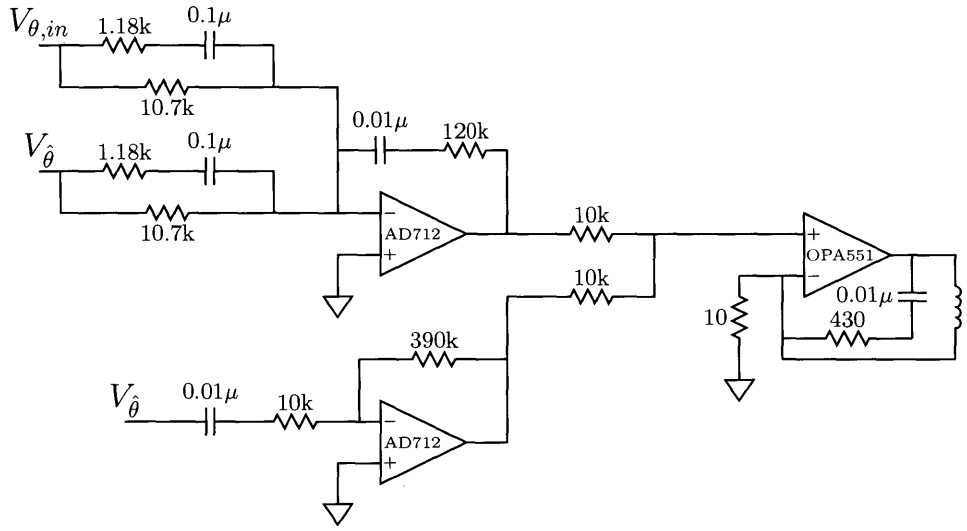

Figure 5.15: Full circuit of the feed-forward lead-lag compensator and drive

5.1.3 Circuit and PCB Construction

Initial circuit design and testing was performed on a bread board. Later, a custom PCB was created. All of the hardware necessary to normalize the quad-cell sensor outputs and provide compensation for the mirror is included on the PCB. Additionally, four mirror mounts were included onto the PCB so that the mirror can be directly mounted to the control board.

The board is powered by a $\pm$12V and ground supply. A LM1117 5V regulator is included to power the mirror quad cell and LED. A four-layer design was chosen. The top and bottom layers are designated to signal routing while the second and third layers provide +12V and ground planes, respectively. All active components were placed on the top layer while all passive components were placed on the bottom. The -12V power supply is routed between the necessary chips on the top layer. All of the components on the board are surface mount with the exception of the AD734 multiplier divider chips, which were only available in DIP packages. Additionally, four mirror mounts were included onto the PCB so that the mirror can be directly mounted to the bottom of the board. A custom board mount was created in order to be able to mount the entire assembly onto an optical table for testing.

The inputs to the board include the power supply rails and inputs to an AD7247 dual-channel parallel 12-bit DAC. The DAC has a total of fifteen digital inputs; 12-bits of parallel data, a write enable pin, a channel A enable pin, and a channel B enable pin. The dual-channel DAC enables both channels to provide outputs while either channel is receiving new digital data.

The dimensions of the board measure 2.25in by 2.25in. Figures 5.16 and 5.17 provide a layout image of the top and bottom board layers, respectively. Figures 5.18 and 5.19 show an assembled board from the top and bottom layer, respectively.

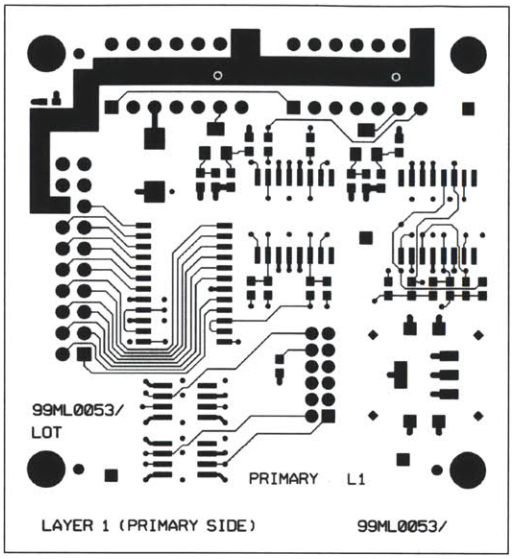

Figure 5.16: Top PCB Layer

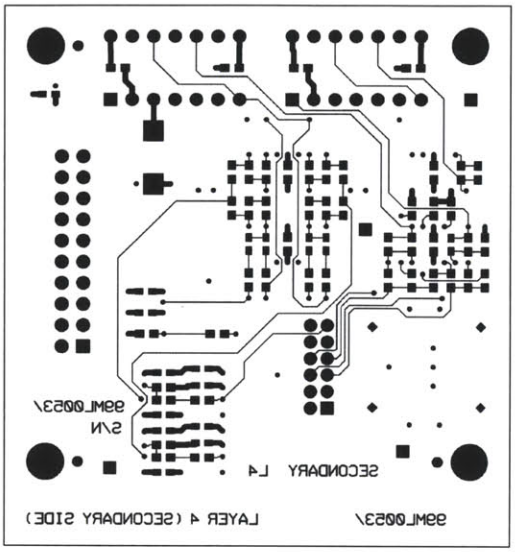

Figure 5.17: Bottom PCB Layer

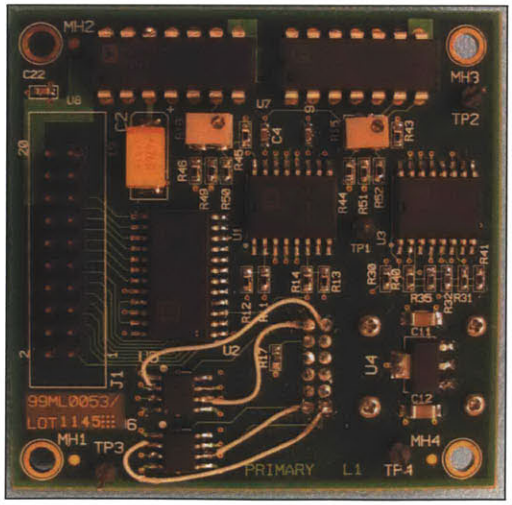

Figure 5.18: Image of assembled top PCB layer

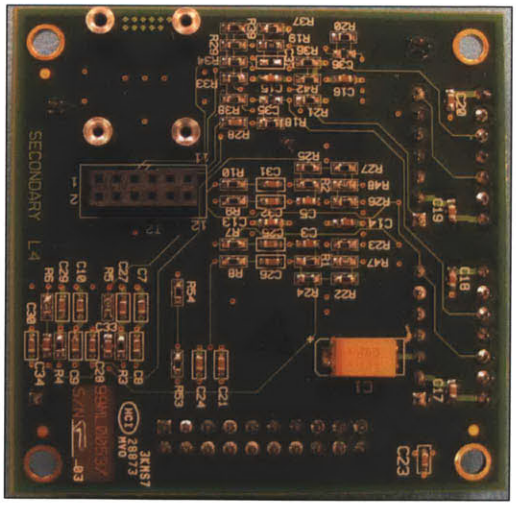

Figure 5.19: Image of assembled bottom PCB layer

5.2 Calibration

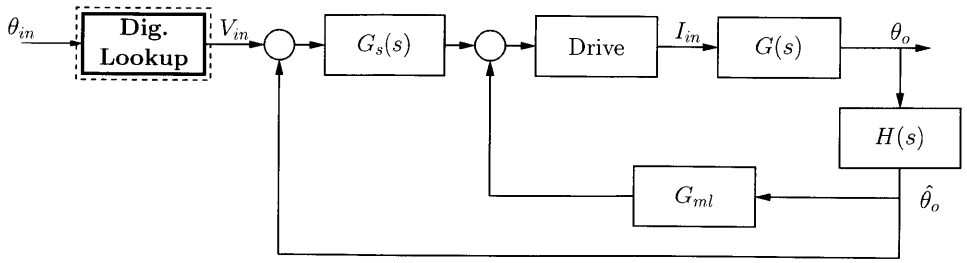

Figure 5.20: Digital look-up table within control system

The compensation described in section 5.1 enables the mirror to move quickly with large low frequency disturbance rejection and with good stability. The control loop is designed to ensure that the input voltage command V_{in} to the compensator matches the IPF voltage outputs $\hat{\theta}_o$ for each axis. Therefore, given a horizontal and vertical voltage command $V_{in,h}$ and $V_{in,v}$, the control loops move the mirror and settle when $\hat{\theta}_{o,h}$ and $\hat{\theta}_{o,v}$ match $V_{in,h}$ and $V_{in,v}$, respectively. In order to command for an angular position, as opposed to IPF voltages, a direct mapping from IPF voltages to their corresponding mirror angle must be constructed.

If the quad-cells were perfectly linear, a simple linear function could be used to map every IPF voltage to a corresponding mirror angle. However, as shown in Chapter 3, the quad-cells exhibit significant nonlinearity. In order to further investigate the nonlinearity of the internal position feedback, the input commands to each axis were scanned over their full IPF range in increments of 24.4mV. By scanning each input over the full IPF range for each axis, the mirror is instructed to move over its full angular range. Figure 5.21 shows the measured IPF values for the horizontal and vertical axes. Figure 5.22 shows the resulting angular position measurements. In each graph, the green and red markers represent the first and last measurements in the scan, respectively.

The effect of the integrator in the compensation loop is that each IPF value will settle to the DC input command with zero error. Therefore, the IPF scan shown in Figure 5.21 follows the input scan commands exactly and as expected, it is a perfect grid with 24.4mV between each vertical and horizontal step.

Looking at the angular scan pattern shown in Figure 5.22, the non-linearities in the internal position feedback become apparent. In some areas, the measured angular positions deviate from a linear approximation by more than 1°. There are a few methods that can be used to compensate for this nonlinearity. The first option is to restrict the angles of operation to a small angular range in which the mapping is fairly linear. This technique follows the traditional method for 'linearization'

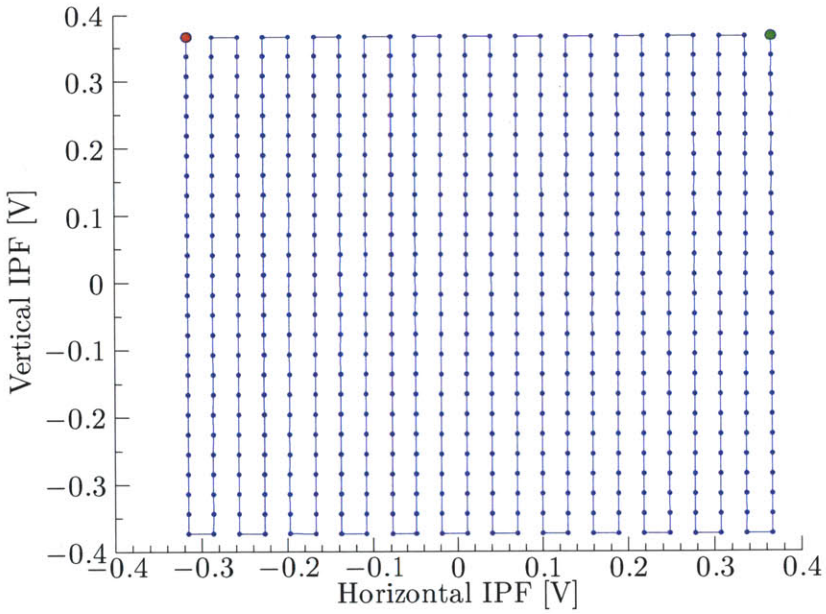

Figure 5.21: Closed-loop IPF input scan pattern

that is commonly used when evaluating circuits. For example, a linear model of a bipolar junction transistor is achieved by assuming small deviations in the base voltage. In order for this technique to work, the operating range of the mirror would have to limited to a fraction of a degree. While this would achieve a nice linear transformation between the IPF sensors and angular position, it would be impractical to limit the range of the mirror to such a small operating range.

The second technique that could be used to compensate for the nonlinearity seen in the quad-cells is to find two 3-dimensional mapping functions that map angular positions of the mirror to measured IPF values. Each 3-dimensional function would map a horizontal and vertical angular command to either a horizontal or vertical IPF value. The IPF value would then serve as the input command to the corresponding axis. This technique offers the benefit of not having to restrict the operating range of the mirror. However, the accuracy of the mapping depends on the number of terms in the polynomials. Fewer terms are easier to compute but provide a very rough estimation of the nonlinearities. Adding terms will result in better estimations but each mapping becomes more difficult to compute. For example, a sample term in the polynomial function would be $\alpha_n x^n$ where n is the order of the term, α_n is a fitted coefficient, and x_n is the desired position. As n increases for higher order terms, evaluating $\alpha_n x^n$ is more prone to saturation or round-off errors, especially if α or x is very large or very small.

The final technique to compensate for the quad-cell nonlinearity that will be discussed is to generate a look-up table that directly maps certain angular positions to certain IPF values. Like a

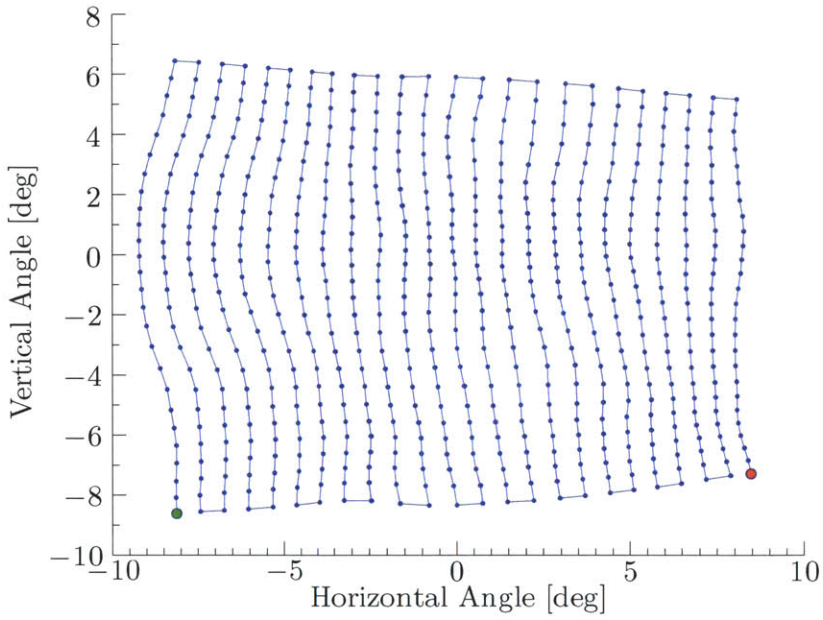

Figure 5.22: Closed-loop position output

mapping function, a look-up table also does not restrict the operating range of the mirror. Compared to a mapping function, a look-up table will take up more memory space but can be customized to provide excellent resolution while maintaining a relatively small size. For example, the digital-to-analog converter used throughout this project offers 12-bit resolution. If every step in the DAC were used in a look-up table, a table would have 16.7 million ($2^{12} * 2^{12}$) entries. However, the look-up table can be downsampled in order to save memory. For example, if the mirror angle for every ten steps of the DAC is stored, the size of each look-up table is reduced by a factor of 100. In order to still maintain high precision, real-time interpolation can be performed. Additionally, the precision of the table can be increased or the size of the table can be decreased by including additional samples in areas that are very nonlinear and decreasing the number of samples in areas that exhibit good linearity.

In order to compensate the for nonlinearity of the quad-cells, a look-up table was generated for its flexibility and relatively straight forward implementation. The table was generated by scanning over the range of the mirror and recording the IPF value for the horizontal and vertical axes as well as the angular position of the beam. A step size of roughly 0.1° was chosen in order to provide good accuracy while maintaining a relatively small table size. With a step size of 0.1°, one complete look-up table contains 40,000 entries.

With all of the measurements taken, the next step is implementing an algorithm to search the look-up table and determine the best set of input commands to move the mirror to a desired angular

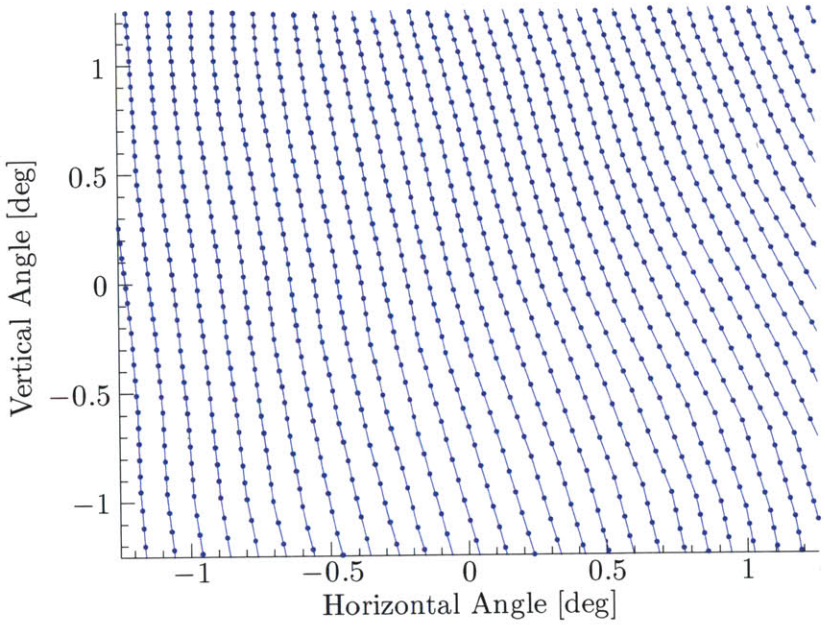

Figure 5.23: Center 2x2 degree closed-loop scan without look-up table

position. The best set of input commands is the set that is most likely to steer the mirror closest to the desired angular position. Since the horizontal and vertical axes are not independent to each other, it is not straight forward to solve the problem one axis at a time. For example, given a desired horizontal angle of 1°, the best command to the horizontal axis can vary significantly depending on the desired vertical angle. Therefore, it becomes necessary to simultaneously consider the desired vertical and horizontal angular position for both the horizontal and vertical input commands. Given a complete look-up table, the brute force technique to finding the best input commands is to compute the distance from each position in the look-up table to the desired angular position and then select the input commands corresponding to the position that minimizes the distance, as expressed by Equation (5.6). In Equation (5.6), h_d and v_d refer to the desired horizontal and vertical angular positions, respectively, while h and v refer to the test points that map to input voltage values.

$$\begin{aligned} R_{in} &= \min_{\mathrm{h,v}}(\sqrt{(\mathrm{h_d}-\mathrm{h})^2+(\mathrm{v_d}-\mathrm{v})^2}) \\ &= \min_{\mathrm{h,v}}((\mathrm{h_d}-\mathrm{h})^2+(\mathrm{v_d}-\mathrm{v})^2) \\ &= \min_{\mathrm{h,v}}(|\mathrm{h_d}-\mathrm{h}|+|\mathrm{v_d}-\mathrm{v}|) \end{aligned} \tag{5.6}$$

This is algorithm is very straightforward to compute within Matlab. The inefficiencies of this algorithm can be seen when considering that the distance to the desired position is calculated for

every single point in the look-up table. If, for example, point A is found to be closer to the desired position than point B, then any points that lie outside the distance of point B should automatically be neglected. This insight leads to the development of a binary search algorithm whereby the look-up table is progressively cut in half according to the areas that lie closest to the desired position. With each step, only the distances between the two center points of each half of the table are compared. The side with the point that falls closest to the desired position is selected and the process is repeated on the nearest half of the table. Each division of the table alternates between a horizontal division and a vertical division until the closest point is isolated. This process is shown graphically by Figure 5.24. The 'x' in the image represents a desired angular position while the dots represent the two test locations. The distance between each test point and the desired position is compared for each step. The side that contains the closer of the two test points is selected while the other side is discarded.

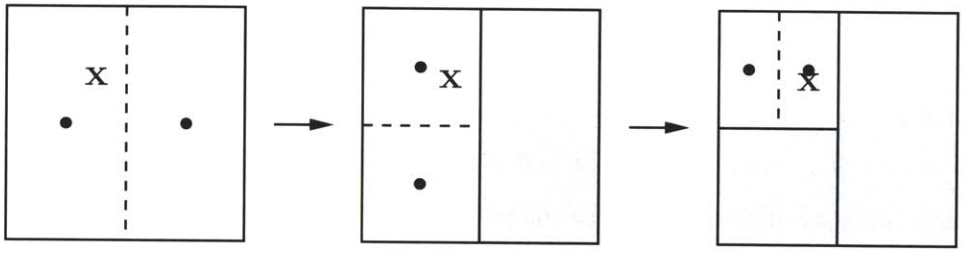

Figure 5.24: Graphical demonstration of a binary look-up table search algorithm

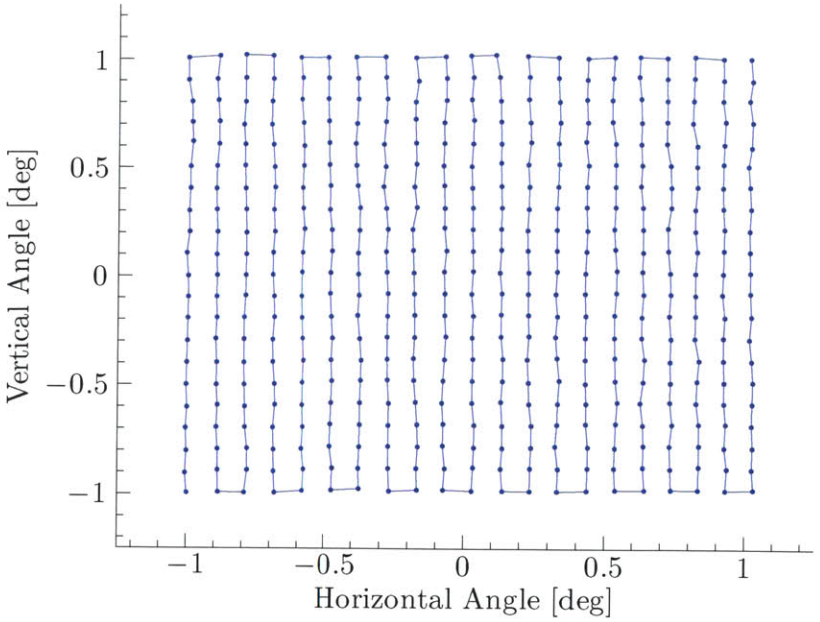

Figure 5.25: Center 2x2 degree closed-loop scan with look-up table

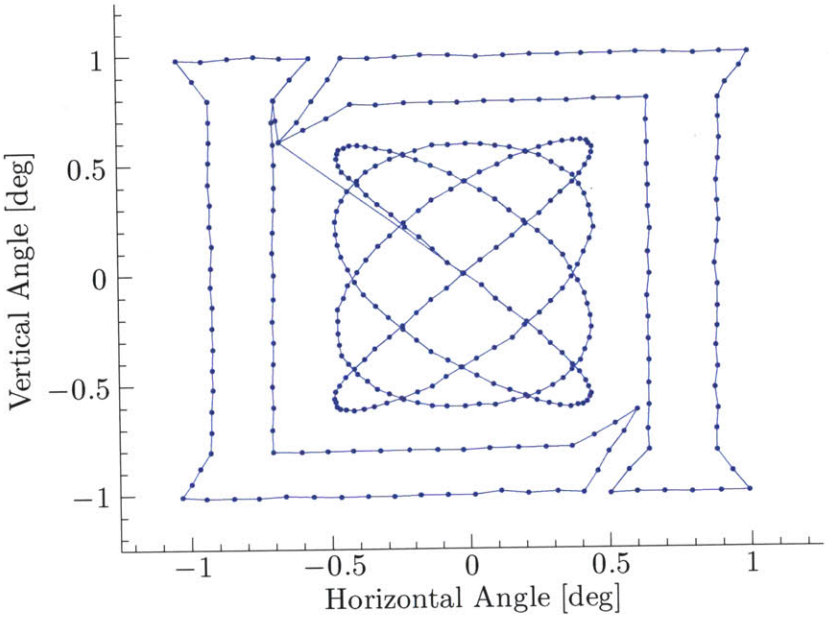

Figure 5.26: MIT Lincoln Laboratory Logo Scan

The running time of the brute force algorithm, given n elements in the look-up table, is $O(n)$. Conversely, the running time of the binary search algorithm is $O(\log_2(\mathrm{n}))$. Given a table consisting of 40,000 entries, this is the difference between comparing 40,000 entries using the brute force algorithm to at most 30 comparisons using the binary search algorithm.

With the look-up table algorithm in place, the mirror is now able to generate command voltages for desired angular positions. Figure 5.25 shows the position measurements of a scan where the mirror was commanded over a 2° by 2° grid in 0.1° increments. Each point on the plot represents a single measurement using the spatial measurement test bench. As can be seen, the estimated position of the beam closely follows the desired grid pattern. A Matlab program was created in order to easily generate arbitrary input commands to the mirror. Figure 5.26 shows a scan of the MIT Lincoln Laboratory logo that was created as a demonstration of capabilities.

5.2.1 Repeatability

The repeatability of the beam positioning is very important for ensuring accurate beam steering performance. As discussed in section 4.1, both the drive coils and quad cells are susceptible to changes in temperature. Variations in temperature will cause the impedance of the drive coils to change. While this will affect the dynamic performance of the mirror, as long as the system does not become unstable, it will not have an effect on the repeatability of the system. The dark current

of each of the four quad cells also changes with variations in temperature. If this effect is not compensated for, it will have an effect on the repeatability of the mirror.

Before compensating for variations in the dark current of the quad cell, it is important to test the repeatability of the system during ideal non-changing conditions. Repeatability is classified as the ability of the mirror to move to the same location given the same set of input commands. In order to measure the repeatability, ten different locations evenly spread across the two dimensional angular range of the mirror were chosen. For each of the ten positions, the mirror was moved back and forth between the origin and the given location ten times. As shown section 3.2, the USB camera contains some variance in the centroid calculations that makes each estimation repeatable to roughly 20μrad. In order to minimize the effect of the variation within each position estimation, fifty different images were taken for each test point. The estimated angular position for each of the fifty images were then averaged together to give one of the ten measurements per location.

The integration of the error in the control loop will ensure that the position feedback values settle to the input voltage commands. The repeatability of the system is therefore largely dependent on the repeatability of the internal quad cell. During regular operation of the quad cell, it is very important that any external sources of light noise be very well controlled. Even normal room lighting generates enough variation in ambient light intensity to have an effect on the internal position feedback. For this reason, repeatability measurements were conducted with all room lighting turned completely off. One solution to this problem is to modulate the LED light at a high frequency. By high-pass filtering the resulting quad cell signals, the effect of any slowly varying light sources will be removed.

The results of the repeatability tests were accumulated by measuring the angular distance from the average position estimation for each of the ten chosen locations. The maximum error from the average location remained under 40μrad while the average error over all ten locations measured less than 10μrad.

The data sheet for the mirror indicates a resolution of 13 bits in the internal position feedback. Given a 20° optical angular range, 13 bits equates to roughly 40μrad of beam steering accuracy. Therefore, the results of the repeatability measurements and the expected performance match well.

If better repeatability is required, it may be possible to implement external hardware to estimate to the position of the mirror. For example, a fraction of the reflected beam could be diverted to an external, high precision quad cell.

Chapter 6

Scan Expansion

The angular range of the mirror is roughly $\pm$ 5° which may not be enough for some applications. For instance, it is often necessary for 3-D laser imaging and optical communication to be able to scan a laser beam over 360° of azimuth and at least 90° of elevation. Discussed in this chapter are a few of the ideas to achieve such range of scan angles.

6.1 Mechanical Mirror Assembly

Compared to traditional mechanical gimbals, MEMS systems have the advantage of relatively high bandwidth and precision but have a relatively small angular range. By combining a mechanical system with a MEMS mirror, it is possible to achieve high resolution, high bandwidth, and large angular ranges. An example concept of this idea is demonstrated in Figure 6.1.

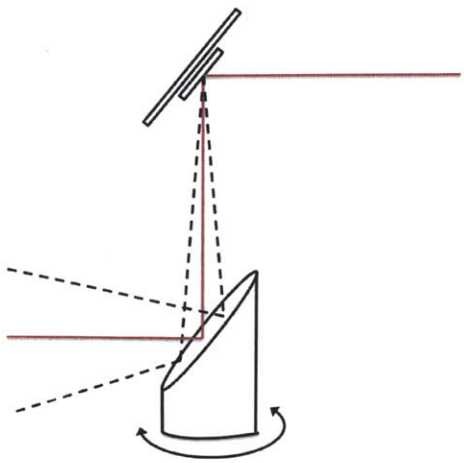

Figure 6.1: General concept of a coarse mechanical beam expansion assembly

In general, the large mechanical assembly can be considered to provide coarse control of the beam position while the MEMS mirror provides fine control. The mechanical mirror tracks large transients in the beam position. Since it is likely that the system will not require very large movements very quickly, the mechanical mirror does not need to be very fast. Also, since the mechanical mirror need only steer to within the range of the MEMS mirror, the mechanical system does not need to have very high resolution.

Figure 6.1 demonstrates a very simple assembly whereby the tilt angle of the mechanical mirror is fixed but the assembly is able to rotate 360° around its vertical axis. The ability to rotate around the vertical axis enables full azimuth range. However, if the mechanical mirror is not able to tilt, the maximum elevation range will only be twice the range of the MEMS mirror. Replacing the mechanical system represented in Figure 6.1 with a full tip-tilt mirror assembly fixes this problem at the cost of extra complexity.

With the mechanical assembly in place, the position of the beam is now being controlled by both the MEMS mirror and the mechanical mirror. This introduces the question of how to synchronize the MEMS system and mechanical system in order to achieve accurate beam steering. First, the total deflection of the beam off both the MEMS and mechanical systems must point the beam to the desired location. Second, the MEMS system should never be forced to the limits of its angular range. Ideally, the MEMS system should be maintained centered around its origin.

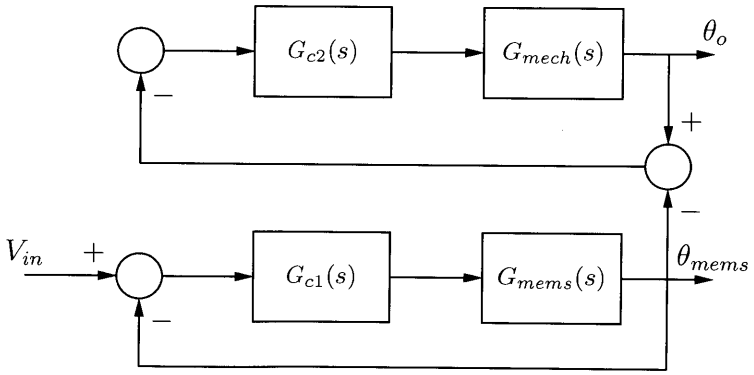

Figure 6.2: Control system for coarse mechanical mirror and fine MEMS mirror

A possible controller design for this system is shown in Figure 6.2. The concept of the controller is to use the difference between the MEMS and mechanical mirror angles to control the movement of the mechanical system. The feedback loop of the MEMS mirror is designed to be much faster than the feedback loop controlling the mechanical mirror. Therefore, if a new input V_{in} is given, the MEMS loop will quickly respond generating a non-zero difference between the mechanical angle, θ_o,

and the angle of the MEMS mirror, θ_{mems}. If the difference is non-zero for long enough, the slower mechanical system will react to try and make the difference zero. In this way, the MEMS mirror is able to compensate for very fast transients while the mechanical system controls larger, slower transients by always trying to move the MEMS mirror back to its origin.

6.2 Scan Expansion Lens

In the previous section, a mechanically actuated mirror was used to expand the angular range of the MEMS mirror. Integrating an additional mechanical assembly may be undesirable for many mobile applications that seek to reduce their size, weight, and power consumption. Another option for achieving a larger angular range is to pass the beam through a passive expansion lens.

A sample angular expansion lens was designed at Lincoln Laboratory. The expansion lens is designed to give roughly a factor of four expansion of the beam angles while preserving the original beam divergence. Its advantageous for the lens not to enlarge the beam divergence in order to maintain high energy densities in the optical signal. Figure 6.3 shows the general concept for the angular expansion lens.

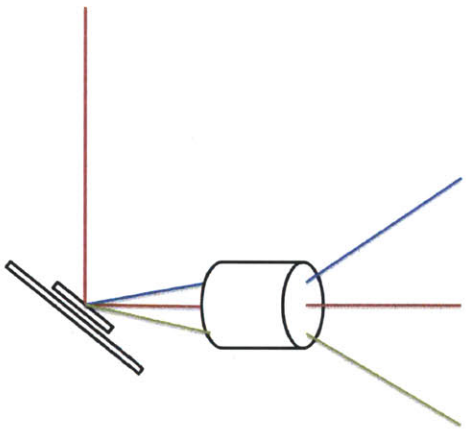

Figure 6.3: General concept of the angle expansion lens

By placing the expansion lens after the MEMS mirror, the effective angular range of the mirror will be increased by the expansion factor of the lens. The advantage of this approach is that it requires no additional power and contributes very little extra volume. However, unlike the mechanical assembly, the expansion lens does not provide full 360° coverage but instead creates a roughly 60° to 80° cone. Multiple MEMS mirror assemblies could be combined in order to achieve full 360° coverage. However, care must be taken to ensure that the coverage cones overlap to ensure that there are no blind spots. The number of required MEMS mirror assemblies will vary with the platform and desired coverage range. This approach then requires controlling which mirror assembly is active at a given time and providing a means to smoothly transition between assemblies. This problem is non-trivial and can quickly lead to significant additional size, weight, and power requirements.

6.3 Reflective Scan Expansion

Another possible approach to achieving angle expansion is to utilize one or more reflective surfaces. If a reflective surface is shaped to be rotationally symmetric, it is possible for a single MEMS mirror to achieve a full 360° of azimuth coverage.

When considering a reflective beam expander, it is important that all of the reflected rays converge to a single point within the reflective volume. This can be achieved by using a hyperbolic reflector with the laser source positioned at the external focal point. Figure 6.4 illustrates the concept with a cross section of a sample hyperbolic reflector.

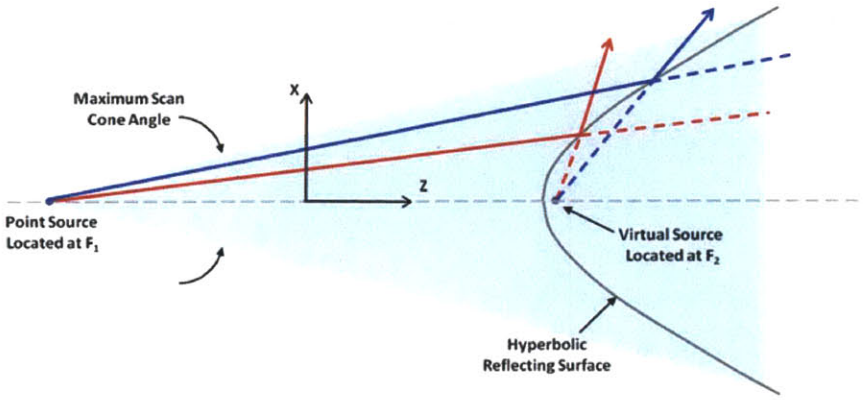

Figure 6.4: Cross section of a hyperbolic reflecting surface

The primary difficulty in utilizing hyperbolic beam reflectors is keeping the beam divergence to acceptable levels while still providing large angular ranges. The amount of beam divergence is dependent on the local radius of curvature of the reflective surface and the spot size of the illuminating beam. A smaller radius of curvature provides greater angular expansion but degrades the beam divergence. As a result, it is advantageous to keep the diameter of the illuminating beam small. If the diameter of the beam is small compared to the radius of curvature of the reflector, then the reflective surface appears relatively flat and the resulting beam divergence is limited. Due to the changing radius of curvature of the hyperbolic surface, the beam divergence is dependent on the scan angle. The worst beam divergence is incurred when the illuminating beam is incident along the dimension of the reflector with the smallest radius of curvature.

A sample configuration employing multiple reflective surfaces is shown in Figure 6.5 as a demonstration of design trades. By utilizing multiple reflective surfaces, the total package volume of the angular expander can be reduced. On the other hand, reflecting the beam off of multiple convex

surfaces introduces further beam divergence. A concave reflecting surface may be able to compensate for this additional divergence.

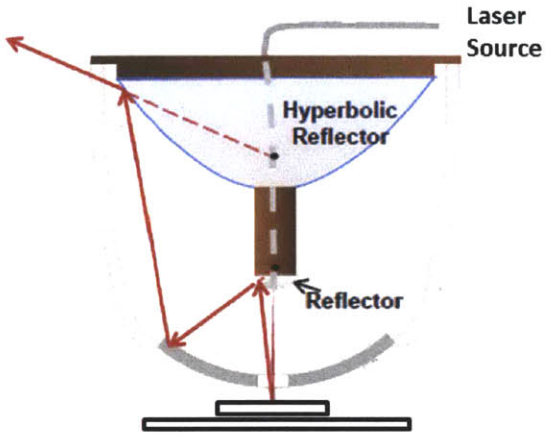

Figure 6.5: Three-surface hyperbolic reflective beam expander

Chapter 7

Improvements and Conclusion

7.0.1 Switching Amplifier

One of the areas that has potential for improvement is the drive electronics for each pair of voice coils. The current method implements a linear amplifier with current mode feedback. The power efficiency of this design can be improved from its current value of roughly 21% by incorporating a switching amplifier. The circuit uses hysteretic control to modulate the current through the voice coils, a technique described as two-state modulation and first developed by Bose in 1963 [16].

The two-state modulation in this circuit is accomplished by an LM311 comparator configured with positive feedback as a Schmitt trigger. Hysteretic control is derived from the fact that the circuit keeps the output voltage V_o within the hysterisis band of the Schmitt trigger. Figure 7.1 shows a schematic of the proposed design. Consider first that the input command V_{com} is zero. If the output of the Schmitt trigger is high at +5V, then the top PFET is on and V_o is set to +12V. At this point, the capacitor C_1 is charging. C_1 charges until its voltage exceeds the hysterisis band of the Schmitt trigger, setting the output of the Schmitt trigger low. If the output of the Schmitt trigger is low, then V_o becomes -12V and the capacitor discharges until its voltage reaches the negative hysterisis band of the Schmitt trigger. If the switching frequency is much faster than the corner frequency of the inductive load, then the charging of C_1 can be considered roughly linear.

When V_{com} is non-zero it provides an extra charging current to C_1, either increasing or decreasing the time required for V_o to transition between the hysterisis bands of the Schmitt trigger. When V_{com} is its maximum voltage, C_1 charges at twice the rate of charge as when V_{com} was zero and discharges only until the voltage on C_1 becomes zero. For intermediate values of V_{com}, the circuit will adjust the rise and fall times, and consequently the switching frequency, to match the average output voltage

with the command. Since the maximum charge slope is only twice the charge slope with zero input, the output pulse width is limited to half of pulse width with zero input. This inherent restriction on the pulse width solves many problems associated with fixed frequency switching amplifiers, including incomplete switching that occurs when the pulse width is exceedingly short. Figure 7.2 shows a demonstration of the output and Schmitt trigger waveforms given a step in V_{com}.

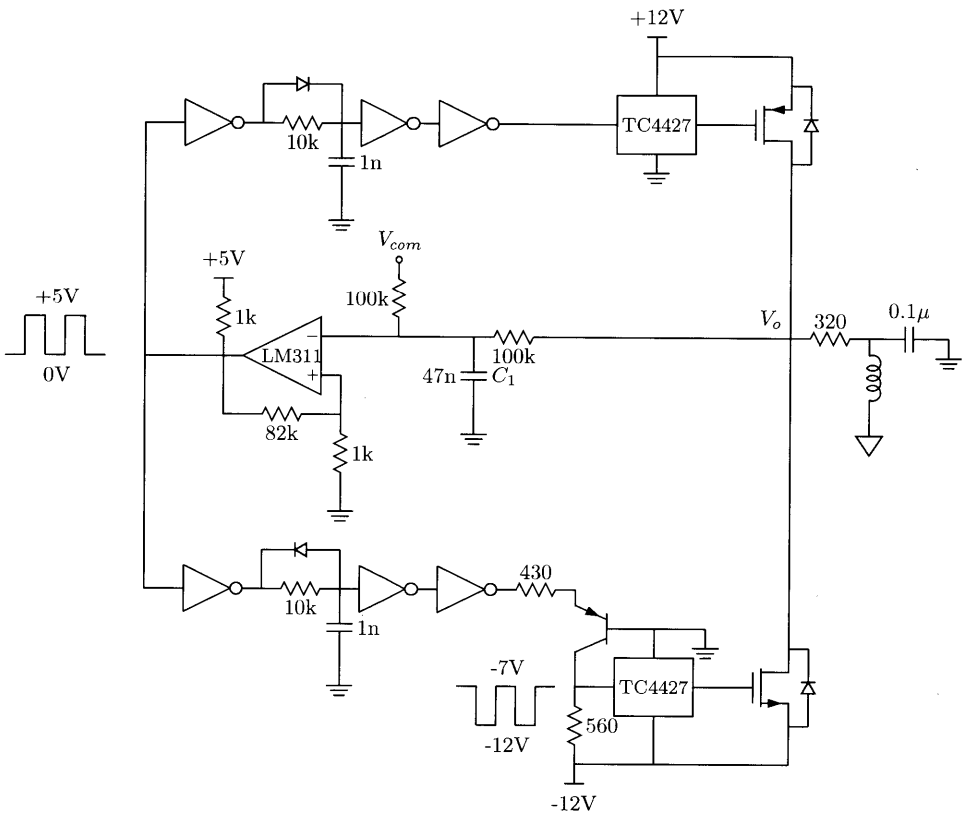

Figure 7.1: Switching amplifier schematic

In order to maintain a linear approximation for the current amplifier, in general the switching frequency of the amplifier should be much higher than the corner frequency of the load. If the switching frequency is fixed, this can simply be designed for. The switching frequency during hysteretic control, on the other hand, varies depending on the load demand. For example, at very high or very low demands, the switching frequency can be dramatically reduced. As the switching frequency is reduced, however, the duty becomes very near to either zero or one creating narrow pulse widths. Therefore, while the switching frequency may become relatively low compared to the corner frequency of the load, the narrow pulse widths ensure relatively small output ripple.

A good rule of thumb for calculating the switching frequency is to sample six to ten times over the rise time of the system. This gives a switching frequency ω_{sw} roughly thirty times the crossover

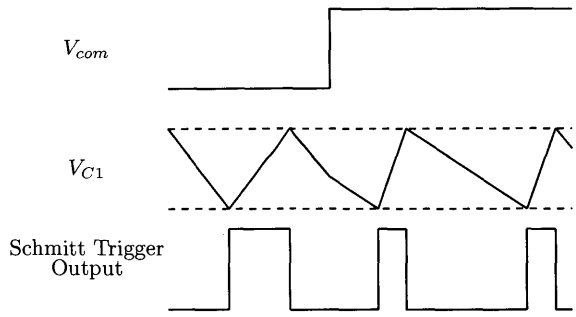

Figure 7.2: Example signal waveform for the hysteretic control switching amplifier

frequency ω_c of the system. The switching delay can be approximated as half of the switch period whereby the resulting phase shift θ_D is given by Equation (7.1).

$$\begin{aligned} \theta_D &= -sT/2 = -\omega_c \pi/\omega_{sw} \\ &= -\pi/30 \text{ rad} \\ &= -6^\circ \end{aligned} \tag{7.1}$$

The corner frequency of the inductive voice coils is measured at 35kHz. Thirty times this frequency results in a switching frequency of over 1MHz, unsuitable for this application. Fortunately, the mechanical time constant of the mirror is roughly 130Hz. Current ripple above this frequency will barely be visible in the movement of the mirror. Still, large current ripple through the voice coils can potentially decrease the efficiency of the amplifier. Therefore, a low pass filter with a corner frequency of 5kHz can be placed in series with the drive coils. Then, the required switching frequency has been decreased to a more reasonable 150kHz.

7.0.2 Digital Control

In addition to implementing a switching current amplifier, another approach to lowering the size, weight, and power specifications of the system is to implement a digital controller. For this application, the sampling rates and resolution (12-14 bits) are well within the range of common digital hardware. The idea of the digital control scheme is to sample and normalize the four quad cell voltages, compare the estimated azimuth and elevation angles to the reference values, pass the difference to a digital controller, and finally input the resulting values to a DAC to interface with the drive circuit. The general block diagram of the feedback and control path of a digital control scheme is

shown in Figure 7.3

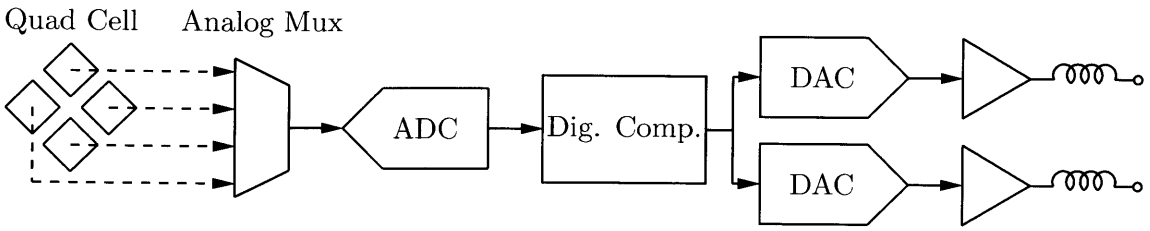

Figure 7.3: Digital compensation block diagram

A single ADC can be used to sample the four quad cell voltages by using an analog multiplexer. This requires that the DAC run four times as fast as would be necessary to sample a single cell. Given that the closed-loop bandwidth of the analog compensator is roughly 2kHz, a reasonable output sample rate is 20kHz resulting in the ADC running at 80kHz. In order to maintain sub-100μrad accuracy in the beam steering system, each component must contain at least 12-bits of resolution.

The analog controller included both minor-loop and feed-forward compensation, the outputs of which are summed and applied as input to the drive circuit for each axis. The same compensation techniques can be implemented in the digital domain by transforming the continuous time transfer functions into discrete time transfer functions. For this problem, the bi-linear or Tustin discretization method is used with a sampling frequency of 20kHz. Equations (7.2) and (7.3) give the continuous time and discrete time transfer functions for the feed-forward lead-lag and minor-loop compensators, respectively.

$$G_c(s) = \frac{1.426 \times 10^{-6}s^2 + 0.002388s + 1}{1.263 \times 10^{-8}s^2 + 1.09 \times 10^{-4}s} \longrightarrow G_c(z) = \frac{97.11z^2 - 186.3z + 89.31}{z^2 - 1.65z + 0.6503} \tag{7.2}$$

$$G_{ml}(s) = \frac{0.0039s}{0.0001s + 1} \longrightarrow G_{ml}(z) = \frac{31.2z - 31.2}{z - 0.6} \tag{7.3}$$

Figures 7.4 and 7.5 compare the frequency response of the continuous and discrete time filters. As shown, the minor-loop and lead-lag discrete filters match well with the continuous compensators out to the sampling frequency.

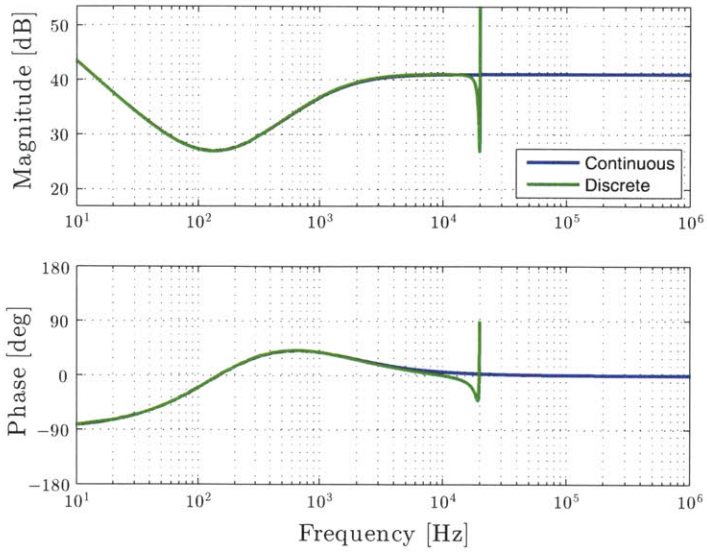

Figure 7.4: Comparison of continuous and discrete frequency responses of the lead-lag compensation network

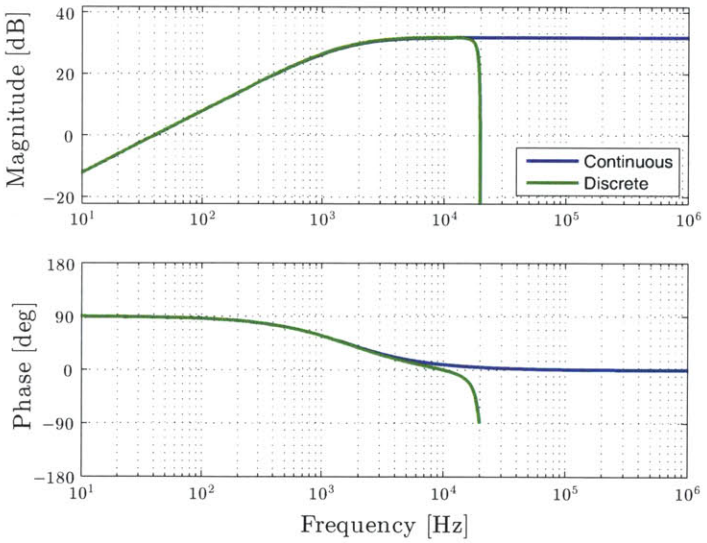

Figure 7.5: Comparison of continuous and discrete frequency responses of the minor-loop compensation network

7.0.3 Conclusion

A control system for a MEMS mirror was designed and implemented to accurately steer a laser beam. First, the behavior of the mirror was accurately measured across both electro-mechanical and optical domains. Through the use of an analog controller, the disturbance rejection and bandwidth of the mirror has been significantly improved. Next, a digital look-up table was created in order to reduce the effects of nonlinear position feedback and enable accurate beam pointing capabilities. Finally, various scan expansion optical and control systems were discussed. Table 7.1 provides a summary of the resulting performance specifications.

Parameter	**Measured**
Closed-loop Bandwidth	1.9kHz
Open-loop Bandwidth	880Hz
Phase Margin	46.8°
Power Consumption	1.1W
Repeatability	$< 40\mu$rad
Lookup Accuracy	250μrad
Board Dimensions	2.25in x 2.25in

Table 7.1: Summary of performance specifications

Bibliography

[1] T. Garlington, J. Babbitt, and G. Long, *Analysis of Free Space Optics as a Transmission Technology*, U.S. Army Information Systems Engineering Command, 2005

[2] JPL Optical Communications Group, www.lasers.jpl.nasa.gov, 09/27/2011

[3] Bell, Alexander G., *On the Production and Reproduction of Sound by Light*, American Journal of Science, Third Series, vol. XX #118, pg. 305-324, October 1880.

[4] D. Boroson, *Channel Capacity Limits for Free-Space Optical Links*, Proc. of SPIE Vol. 2951, 2008

[5] V. Chan, *Free-Space Optical Communications*, Journal of Lightwave Technology, Vol. 24, No. 12, December 2006

[6] G. C. Loney, *Design of a Small-Aperture Steering Mirror for High Bandwidth Acquisition and Tracking*, MIT Lincoln Laboratory, Group 71, Optical Engineering, Volume 29 Number 11, 1990

[7] D. Bayat, *Large Hybrid High Precision MEMS Mirrors*, Ecole Polytechnique Federale De Lausanne Doctorate Thesis, 2011

[8] V. Nikulin, R. Khandekar, *Demonstration of a Mobile Tracking System for Laser Communications*, Convention of Electrical and Electronics Engineering in Israel, 2010.

[9] L. Zhou, M. Last, V. Milanovic, J. Kahn, K. Pister, *Two-Axis Scanning Mirror for Free-Space Optical Communication between UAVs*, IEEE/LEOS Optical MEMS, Aug. 2003.

[10] V. Milanovic, G. Matus, D. McCormick, *Gimbal-Less Monolithic Silicon Actuators for Tip-Tilt-Piston Micrometer Applications*, IEEE Journal of Selected Topics in Quantum Electronics, Vol. 10, No. 3 May/June 2004

[11] Texas Instuments, TALP1000B Dual-Axis Analog MEMS Pointing Mirror, Sept. 2009

[12] Roberge, James K., "The Mechanical Seal", Bachelor's Thesis, Massachusetts Institute of Technology, 1960.

[13] Lundberg, Kent H., empphInternal and External Op-Amp Compensation: A Control-Centric Tutorial, American Control Conference, 2004.

[14] Griffiths, David *Electrodynamics: Introduction to Electrodynamics, 3rd Edition*, Upper Saddle River, New Jersey: Prentice Hall, pg. 286

[15] NewView 7100 Specification Manual, Zygo Corporation, 2010

[16] Bose, A. G., *A Two-State Modulation System*, Wescon Convention Record, Part 6, Paper 7.1, 1963